Dynamical X-ray diffraction theory: Characterization of defects and strains in as-grown and ion-implanted garnet structures

S. I. Olikhovskii*,1, V. B. Molodkin1, O. S. Skakunova1, E. G. Len1, Ye. M. Kyslovskyy1, T. P. Vladimirova1, O. V. Reshetnyk1, E. V. Kochelab1, S. V. Lizunova1, V. M. Pylypiv2, B. K. Ostafiychuk2, and O. Z. Garpul2

[1] G. V. Kurdyumov Institute for Metal Physics, N.A.S. of Ukraine, 36 Academician Vernadsky Blvd., 03142 Kyiv, Ukraine
[2] Vasyl Stefanyk Precarpathian National University, 57 Shevchenko Str., 76025 Ivano-Frankivsk, Ukraine

The generalized dynamical theory of X-ray diffraction by imperfect single crystals is extended to characterize structure imperfections of real single crystals with complex basis and similar crystalline films with inhomogeneous strain fields. The influence of various defects (intrinsic and extrinsic point defects, nanoclusters, and microdefects), simultaneously presented in such structures, on changing both average and fluctuating strain fields as well as structure factors are taken into account. The analytical expressions connecting immediately the coherent and diffuse components of the scattering intensity with statistical characteristics of these defects are obtained. Thus, the self-consistent description of the coherent and diffuse dynamical diffraction intensity components is provided. Some examples of the application of the developed theoretical model to treat rocking curves measured from various garnet structures by using high-resolution double-crystal X-ray diffractometer are reviewed. Possibilities for the quantitative characterization of structural defects and strain profiles in the as-grown and ion-implanted garnet single crystals and yttrium iron garnet films are demonstrated.
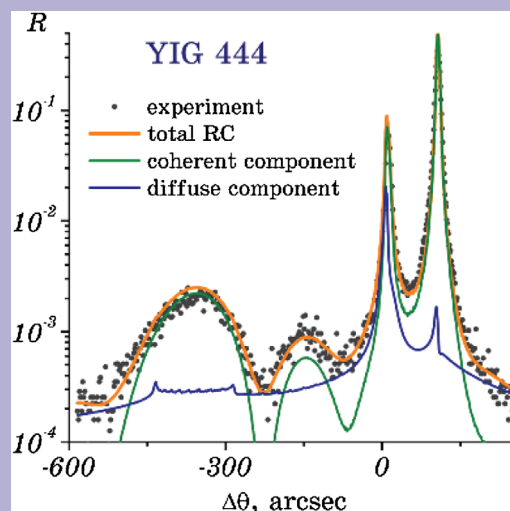
The self-consistent dynamical description of coherent and diffuse scattering intensities from imperfect crystal structures with inhomogeneous strain fields and randomly distributed defects make it possible to determine the parameters of strain profiles and statistical characteristics of defects by analytical treating the coherent and diffuse components of rocking curves measured by the high-resolution double-crystal X-ray diffractometer with widely open detector window.

1 Introduction The nondestructive X-ray diffraction techniques are widely used to determine characteristics of structural defects and strains in the as-grown and modified crystals, multilayer systems, superlattices, and film

structures [1–4]. In particular, the measurement of rocking curves by the high-resolution double-crystal diffractometer (DCD) in Bragg diffraction geometry is one of the most used experimental methods. Effectiveness of this X-ray diffraction method to large extent is determined by its high sensitivity to defects with very small radii down to point defects. This advantage arises due to the integration of diffuse scattering intensity over the horizontal and vertical divergences, on the one hand, and by the availability of the analytical expressions, which give an adequate description of the measured rocking curves, on the other hand.

The various theoretical models of X-ray diffraction, which are based on both kinematical and dynamical scattering theories [5, 6], have been proposed to analyze the rocking curves and reciprocal space maps measured from perfect or imperfect crystalline structures with inhomogeneous strain distributions [1–4, 7–9]. In particular, the generalized dynamical theory of X-ray diffraction by imperfect single crystals with randomly distributed Coulomb-type defects has been developed [10, 11]. This theory is based on the Ewald–Bethe-Laue approach [6] and makes use of the Krivoglaz's method of fluctuating waves of defect concentration which enables for establishing the direct analytical relationships between Fourier components of fluctuating part of crystal polarizability and defect characteristics [5]. The solution of wave equation in a tmomentum space provides the explicit analytical expressions for coherent and diffuse scattering amplitudes directly connected with defect characteristics. Thus, the self-consistent description of the coherent and diffuse components of diffraction patterns measured from imperfect crystal structures can be achieved, particularly, those of the rocking curves measured by the high-resolution DCD with widely open detector window [12].

The choice of the as-grown and ion-implanted synthetic garnet crystals and films as our investigation objects was caused by the circumstance that many functional materials used in modern devices have a complicated multicomponent structure including also the structural imperfections and inhomogeneous strain distributions, which can substantially influence their physical properties (see, e.g., Refs. [13–16]). On the other hand, the synthetic garnet systems themselves are of great interest for both basic scientific research [17–23] as well as various practical applications in magnetic, optical, and magneto-optical devices, etc. [24–27] due to the wide range of variations of their nearly perfect crystalline structure and related physical properties.

The synthetic garnet single crystals have general chemical formula $C_3A_2(DO_4)_3$, where C, A, and D denote cations placed in dodecahedral {c}, octahedral [a], and tetrahedral (d) sites, respectively, and O are oxygen anions located at the corners of corresponding polyhedra. The garnet structure belongs to the space group Ia3d (O_h^{10}), its body-centered unit cell is one of the most complicated among known crystal structures with cubic symmetry and contains eight formula units, i.e., 160 atoms (see, e.g., Ref. [28] and references therein). Such structure provides the possibility to form during growth the solid solutions with other chemical elements by substituting C, A, and D cations in a wide range of their compositions and thus to modify the physical properties connected with garnet crystal structure [29–32].

Another way to control the physical properties of garnets is the use of ion implantation for purposeful modifying the structure of crystal volume or subsurface layers [33–39]. This effective technique provides, due to use of proper ion species and ion energies, the possibility to tailor the optical, magneto-optical, magnetic, and electrical properties of multilayer semiconductor structures, magnetic films, etc. Besides the effect of doping, the influence of defect creation and diffusion, amorphization and intermixing, which occur during ion irradiation, is of significant importance for the formation of crystalline microstructure and strain fields.

The purpose of the present paper is to describe the extension of the generalized dynamical theory of X-ray diffraction in imperfect crystals with Coulomb-type defects to the case of real crystals and crystalline films with inhomogeneous strain fields and complex structure basis. The corresponding method proposed for the determination of structural characteristics of such inhomogeneous crystal structures containing randomly distributed point defects and microdefects makes use of the rocking curves measured by means of the high-resolution DCD in Bragg diffraction geometry. The application of this method will be reviewed on several examples of the characterization of structural defects and strain profiles in the as-grown and ion-implanted gadolinium gallium garnet (GGG), neodymium gallium garnet (NdGG) single crystals, and yttrium iron garnet (YIG) film grown on GGG substrate.

The article has the following structure. In Section 2, the experimental details of performed X-ray diffraction measurements are described. In Section 3, a short historical review on the characterization of ion-implanted crystals by X-ray diffraction methods is presented.

In Section 4, the basic analytical expressions of the generalized dynamical theory for the coherent and diffuse reflection coefficients are described with respect to imperfect garnet single crystals (Section 4.1), films (Section 4.2), and ion-implanted garnet crystals and films (Section 4.3). In particular, the generalized expressions are represented for the diffraction parameters of imperfect multicomponent garnet crystals with taking the influence of defects into account.

The examples of the characterization of microdefects, point defects, and strains in the investigated as-grown and ion-implanted GGG and NdGG single crystals, and single-crystalline YIG film on GGG substrate by using the formulas of the developed dynamical X-ray diffraction model for the analysis of the measured rocking curves are described in Section 5.

The obtained results are discussed in Section 6 and short resume and general conclusions are given in Section 7.

2 Experimental

2.1 Samples The investigated single crystalline GGG and NdGG samples were prepared by using wafers cut from the central part of Czochralski-grown ingots with [111] growth axis.

Epitaxial single crystalline (111) YIG films of 5.33 μm thickness were grown on both sides of 500 μm thick GGG substrate by using liquid phase epitaxy. The Pb impurity content in YIG film was measured to be nearly 0.31 at.%. After lapping, the samples were polished mechanically, chemo-dynamically, and chemically.

The set of the investigated GGG and YIG film samples, which were identical with the as-grown samples described above, has been implanted with 90 keV F^+ and Si^+ ions at various doses between 8×10^{12} and 2×10^{14} cm^{-2}. The angle between the direction of the ion beam and the film surface was kept at $7°$ to avoid channeling effects. The implantation current was 2×10^{-5} A.

2.2 Experimental setup Rocking curves of the investigated samples were measured by using the high-resolution four-circle X-ray DCD with Cu tube (25 kV × 25 mA). Two flat germanium monochromator crystals with symmetrical 333 reflections in the antiparallel setting were used to prepare an incident X-ray beam with suppressed σ component of polarization.

The symmetrical 444 and 888 reflections were used at the samples under investigation, which were in the parallel setting relatively to the last reflection of the monochromator. Rocking curves of the samples were measured by using a step motor controlled by computer in steps of 1.0 arcsec. The statistics of data collection provided the relative measurement errors varied between 3 and 5%.

2.3 Instrumental function The X-ray intensity reflected by the investigated sample in the high-resolution DCD with parallel setting of the investigated sample with respect to the last reflection in the monochromator system can be approximately represented as the onefold convolution of the instrumental resolution function with reflection coefficient of the sample [12]:

$$R(\Delta\theta) = \frac{P^{(\sigma)}(\Delta\theta) + P^{(\pi)}(\Delta\theta)}{P_0^{(\sigma)} + P_0^{(\pi)}},$$

$$P^{(\sigma,\pi)}(\Delta\theta) = \int du V^{(\sigma,\pi)}(u) R_S^{(\sigma,\pi)}(u + \Delta\theta),$$

$$P_0^{(\sigma,\pi)} = \int_{-\infty}^{\infty} du V^{(\sigma,\pi)}(u),$$

where $R_S^{(\sigma,\pi)}$ is the reflectivity of the sample for σ and π polarizations, respectively, and the instrumental function

$V^{(\sigma,\pi)}$ of DCD is calculated for each reflection by the integration the product of first and second monochromator crystal reflectivities with the function describing the line shape of characteristic X-ray radiation over wavelength and vertical divergence [12]. This simplified relationship is used in fitting procedure to decrease the calculation time.

2.4 Data treatment To estimate the fit quality when considering the treatment of measured rocking curves by using the trial-and-error method, both ordinary and weighted agreement factors were used:

$$R = \sum_j \left| R_j^{calc} - R_j^{meas} \right| \Big/ \sum_j R_j^{meas},$$

$$R_w = (N - p)^{-1} \sum_j \left| R_j^{calc} - R_j^{meas} \right| \Big/ R_j^{meas},$$

where $j = \overline{1, N}$, R_j^{meas} and R_j^{calc} are the measured and calculated reflectivities at the angular positions $\Delta\theta_j$ of the sample, respectively, N and p are the numbers of measurement points and fit parameters, respectively. These factors have been found for best fits to vary between 5 and 10% at all the data treatments described below in Section 5. Consequently, the corresponding relative errors of the fit parameters given in Tables 2–8 should be estimated as not worse as 10%.

3 Characterization of ion-implanted crystals by X-ray diffraction methods In the early investigations with using X-ray diffraction to study the structure imperfections generated in the crystals, which were irradiated with neutrons, electrons, or γ-rays, the measurements of only the one-dimensional diffuse scattering intensity distributions were performed by using DCD with conventional X-ray tube (see, e.g., Refs. [5, 40–43]). The interpretation of the corresponding rocking curve tails measured from irradiated metals and semiconductors was based on the kinematical theory [5, 44–46]. The use of relatively simple kinematical formulas was possible due to the wide diffuse scattering intensity distributions from point defects and small point defect agglomerates, dislocation loops, or precipitates, which sizes ranged from the atomic level up to hundreds of nanometers, i.e., were significantly smaller as compared with the extinction length defining the width of the Bragg peak. The relative changes of an average crystal strain due to the radiation defects distributed randomly in the crystal bulk were determined by lattice parameter measurements.

The appearance of modern power X-ray sources, namely, X-ray tubes with a rotating anode and synchrotron radiation facilities, provided the possibility for the wide use of triple crystal diffractometers to measure reciprocal space maps and, consequently, in more details analyze the complicated displacement fields caused by various

configurations of radiation-induced defects. Such diffuse scattering measurements, in combination with substantially increased computing power, made it possible to perform the investigations with using the atomistic simulation methods by which the diffuse X-ray scattering can be calculated for an arbitrary finite-sized defect in any material where reliable interatomic force models exist [47–51].

The availability of high intensity X-ray sources has opened an opportunity for the diffraction techniques with grazing incidence and exit angles, extremely asymmetrical X-ray diffraction, X-ray reflectivity, X-ray micro-diffraction in Laue mode, etc., to be widely applied for the study and characterization of strain, damage, and defects in thin subsurface layers of ion-implanted crystals [52–59]. Moreover, there became possible such X-ray diffraction experiments as mapping lattice distortions perpendicular to the surface in patterned silicon samples after implantation of low energy ions as a function of depth and lateral position with sub-micrometer resolutions by using triple-crystal X-ray diffractometry data [60]. Also, the unique depth-resolved measurements by using the focused synchrotron X-ray beam of sub-micrometer resolution have been performed to study of size, type, and depth distribution of defect clusters created in silicon after implantation of high-energy Si ions [61].

Since the ion implantation became a routine tool for purposeful modifying the structure of subsurface crystal layers, the various theoretical models have been developed to describe the X-ray diffraction patterns, in particular, the rocking curves measured from such crystal structures with inhomogeneous strain fields. In whole, the most of these models could be subdivided into two groups, which make use of the semi-kinematical [62–70] or dynamical approximations [7, 71–74], respectively. The first group of so-called semi-kinematical (or known also as kinematical [65]) models is characterized by the summation of kinematical scattering amplitudes from thin ion-implanted layers and dynamical scattering amplitude from a thick substrate. Thus, their interference is taken into account when the reflected intensity is calculated. In fully dynamical models, the recurrence relations are used between analytical solutions of dynamical theory for the wave amplitudes in imaginary thin crystal layers (laminae) with constant strain in each lamina. These analytical solutions have been obtained from both Takagi–Taupin equations in real space and wave equation in momentum space according to the Ewald–Bethe-Laue approach, supposing the lamina are defect-free and diffuse scattering is absent (except for Ref. [74]).

In general, the inverse scattering problem for the determination of an arbitrary strain profile by using measured rocking curves is too complicated to be solved unambiguously in the simple analytical terms (cf., e.g., Ref. [75]). For this reason, the numerical methods for the solution of the inverse scattering problem are still improved. For example, a novel least-squares fitting procedure was presented that allows the retrieval of strain and damage profiles in ion-implanted single crystals using rocking curves from high-resolution X-ray diffraction measurements [70, 76]. Besides, such numerical approaches have been developed, as the recognition method using the principle of neural network to treat high-resolution X-ray diffraction data [77], and the optimization method known as the genetic algorithm, which was adapted to fit experimental data obtained for ion-implanted crystals to simulated rocking curves [78].

It is important to remark that in most of the above-mentioned approaches, the disorder created by radiation defects in the implanted layer is taken into account only as amorphization factor (static Krivoglaz–Debye–Waller factor) in coherent scattering amplitude. At the same time, the existence of diffuse scattering effects from defects in both the implanted layer and crystal bulk is ignored and, consequently, their influence on the characterization results is neglected.

Below, in Section 4, we describe shortly the main features of the generalized dynamical theory of X-ray diffraction in imperfect single crystals with randomly distributed defects [10–12] and its extension to the case of ion-implanted crystals including multicomponent compounds. The proposed approach allows for the adequate analytical description of both the coherent and diffuse scattering intensities from such crystal structures.

4 Generalized theory of dynamical X-ray diffraction for imperfect garnet crystals

4.1 Reflectivity of imperfect crystal

4.1.1 Coherent component of reflectivity
Real single crystals always contain growth defects as well as intrinsic and extrinsic point defects. The complexity of their influence on both coherent and diffuse components of the scattering intensity is substantially increased in multicomponent crystalline compounds like garnets due to the rising diversity of various defect structures which modify the diffraction parameters.

The dynamical coherent component of the reflectivity of the imperfect thick crystal which contains randomly distributed defects is described in the two-beam case of Bragg diffraction geometry by the following expressions [12]:

$$R_{\mathrm{coh}}(y) = |r_{\mathrm{B}}(y)|^2,$$

$$r_{\mathrm{B}}(y) = \sqrt{\zeta}\Big[y - \mathrm{sgn}(y_{\mathrm{r}})\sqrt{y^2 - 1}\Big], \tag{1}$$

$$y = (\alpha - \alpha_0)\sqrt{b}/\sigma, \quad \alpha = -\Delta\theta\sin(2\theta_{\mathrm{B}}), \tag{2}$$

$$\alpha_0 = [\chi_0 + \Delta\chi_{\mathbf{HH}} + (\chi_0 + \Delta\chi_{00})/b]/2, \tag{3}$$

$$\sigma^2 = (CE\chi_{\mathbf{H}} + \Delta\chi_{\mathbf{H}0})(CE\chi_{-\mathbf{H}} + \Delta\chi_{0\mathbf{H}}), \tag{4}$$

Original

Paper

Phys. Status Solidi B (2017)   (5 of 22) 1600689

$$\zeta = (CE\chi_{\mathbf{H}} + \Delta\chi_{\mathbf{H}0})(CE\chi_{-\mathbf{H}} + \Delta\chi_{0\mathbf{H}})^{-1}. \qquad (5)$$

Here $y_r = \mathrm{Re}\, y$, $\Delta\theta$ is an angular deviation of the investigated crystal from its exact Bragg position, θ_B is the Bragg angle, C is the polarization factor equal to 1 or cos $(2\theta_B)$ for σ and π polarization, respectively. Also, $\chi_{\mathbf{G}}$ is Fourier component of the perfect crystal polarizability $(\mathbf{G} = \mathbf{0}, \pm\mathbf{H})$, $b = \gamma_0|\gamma_{\mathbf{H}}|^{-1}$ is the parameter of diffraction asymmetry, γ_0 and $\gamma_{\mathbf{H}}$ are direction cosines of the wave vectors of incident and diffracted plane waves, respectively, $E = \exp(-L_{\mathbf{H}})$ is the static Krivoglaz–Debye–Waller factor, and $\Delta\chi_{\mathbf{GG}'}$ are complex dispersion corrections due to diffuse scattering ($\mathbf{G}$ and $\mathbf{G}' = \mathbf{0}$ or $\mathbf{H}$, where $\mathbf{H}$ is the reciprocal lattice vector).

The static Krivoglaz–Debye–Waller factor and dispersion corrections due to diffuse scattering can be calculated for typical microdefects by using known relations. Namely, the exponent of static Krivoglaz–Debye–Waller factor for dislocation loops with randomly oriented Burgers vector $\mathbf{b}$ is described by the following expression [5]:

$$L_{\mathbf{H}} \cong 0.5\, n_L R_L^3 (H|\mathbf{b}|)^{3/2}, \qquad (6)$$

where $n_L = c_L/v_c$ and c_L are number density and concentration of dislocation loops, respectively, $v_c = a^3$ is the unit cell volume, and R_L is dislocation loop radius.

For spherical amorphous clusters or new phase particles, the similar approximate formula has been obtained in the approximation of elastically isotropic continuum [79]:

$$L_{\mathbf{H}} \cong \begin{cases} 0.525 n_C v_c n_0 \eta^4, & \eta \leq 1.9, \\ n_C v_c n_0 \eta^3, & \eta > 1.9, \end{cases} \qquad (7)$$

$$\eta = \sqrt{\Gamma|\varepsilon|HR_C}, \quad n_0 = 4\pi R_C^3/(3v_c),$$

$$\Gamma = (1 + \nu)[3(1 - \nu)]^{-1},$$

where $n_C = c_C/v_C$ is the number density of clusters, ε is the linear strain at cluster interface, ν is the Poisson ratio, and R_C is the cluster radius.

The complex dispersion corrections due to diffuse scattering can be calculated by using the approximate relations with the coefficient of absorption due to diffuse scattering [12]:

$$\Delta\chi_{\mathbf{GG}} = P_{\mathbf{GG}} - i\mu_{\mathbf{GG}}/K, \qquad (8)$$

$$P_{\mathbf{GG}} \approx -\mu_{\mathbf{GG}}/K, \qquad (9)$$

$$\mu_{00}(\Delta\theta) \approx b\mu_{\mathbf{HH}}(\Delta\theta) \approx b\mu_{ds}(\Delta\theta), \qquad (10)$$

where $K = 2\pi/\lambda$ is the module of the wave vector $\mathbf{K}$ of an incident plane wave, λ is X-ray wavelength, and $\mathbf{G} = \mathbf{0}, \mathbf{H}$. The non-diagonal dispersion corrections to the wave vectors of coherent waves can be neglected for typical microdefects with the effective radii significantly smaller than extinction length, i.e., for such microdefect sizes one can put:

$$\begin{aligned} P_{\mathbf{0H}}(\Delta\theta) &\approx P_{\mathbf{H0}}(\Delta\theta) \approx 0, \\ \mu_{\mathbf{0H}}(\Delta\theta) &\approx \mu_{\mathbf{H0}}(\Delta\theta) \approx 0. \end{aligned} \qquad (11)$$

The coefficient of absorption due to diffuse scattering $\mu_{ds}(\Delta\theta)$ is connected with the same defect characteristics as the static Krivoglaz–Debye–Waller factor, on the one hand, and diffuse component of the crystal reflectivity, on the other hand (see below).

4.1.2 Generalized diffraction parameters

According to the generalized dynamical theory of X-ray diffraction in imperfect crystals with randomly distributed defects the conventional diffraction parameters for perfect crystals, as can be seen from Eqs. (1)–(5), are modified by introducing the static Krivoglaz–Debye–Waller factor and dispersion corrections due to diffuse scattering [10, 12]. Thus, the generalized diffraction parameters can be defined instead of the Fourier components of perfect crystal polarizability as follows:

$$\begin{aligned} \tilde{\chi}_0 &= \chi_0 + \left(b^{-1} + 1\right)^{-1}\left(b^{-1}\Delta\chi_{00} + \Delta\chi_{\mathbf{HH}}\right), \\ \tilde{\chi}_{\mathbf{H}} &= E\chi_{\mathbf{H}} + C^{-1}\Delta\chi_{\mathbf{H0}}, \\ \tilde{\chi}_{-\mathbf{H}} &= E\chi_{-\mathbf{H}} + C^{-1}\Delta\chi_{0\mathbf{H}}, \end{aligned} \qquad (12)$$

The transformation of the diffraction parameters into the generalized ones due to microdefects is realized, as can be seen from Eq. (12), via static Krivoglaz–Debye–Waller factor $E = \exp(-L_{\mathbf{H}})$ and dispersion corrections due to diffuse scattering $\Delta\chi_{\mathbf{GG}'}$. At the same time, it is important to note that Fourier components of the multicomponent garnet crystal polarizability $\chi_{\mathbf{G}}$ in Eq. (12) are not referred to the perfect crystal structure but should be additionally modified to account for point defect configurations like substitutional or antisite defects, and thus will depend on point defect characteristics. At the same time, the static Krivoglaz–Debye–Waller factor and dispersion corrections due to diffuse scattering depend on both microdefect and point defect characteristics.

Besides, Fourier components of the crystal polarizability are dependent not only on the crystal structure factors but on the unit cell volume as well. This volume is changed with concentrations of point defects and is expressed through the corresponding cubic lattice parameter of rare-earth garnets. The later can be found in accordance with crystal-chemical calculations by using the empiric analytical expression [80, 81]:

$$a = b_1 + b_2 r_{\rm c} + b_3 r_{\rm a} + b_4 r_{\rm d} + b_5 r_{\rm c} r_{\rm a}$$
$$+ b_6 r_{\rm c} r_{\rm d} \; \left(\overset{\circ}{\rm A} \right), \tag{13}$$

$$r_i = \sum_j g_{ij} r_j, \tag{14}$$

$$b_1 = 7.02954, \quad b_2 = 3.31277, \quad b_3 = 2.49398,$$

$$b_4 = 3.34124, \quad b_5 = -0.87758, \quad b_6 = 1.38777,$$

where $r_{\rm c}$, $r_{\rm a}$, and $r_{\rm d}$ are weighted effective ionic radii of cations (in Å), that occupy accordingly dodecahedral {c}, octahedral [a], and tetrahedral (d) positions in the garnet crystal structure, g_{ij} is a portion of sort j ions with a radius r_j in crystallographic ith position.

Dependencies of the Fourier components of polarizability on concentrations of point defects calculated for YIG 000, 444, and 888 reflections of $CuK\alpha_1$ radiation are shown in Fig. 1 [82]. It is remarkable that these dependencies have different, in some cases opposite, behavior for different reflections what can be important at the diffractometric refinement of point defect characteristics.

To provide the self-consistency of the proposed diffraction model, the change of crystal lattice parameters and, consequently, Fourier components of crystal polarizability not only due to point defects but also due to microdefects should be taken into account. For the most simple models of spherical clusters or new phase particles and randomly oriented prismatic dislocation loops the change of crystal lattice parameter $\Delta a/a_0$ and the corresponding changes of cubic unit cell volume $\Delta v_{\rm c}/v_{\rm c}$, i.e., the additional volume strains $\varepsilon_{\rm C}$ and $\varepsilon_{\rm L}$, respectively, are described by following expressions [5]:

$$\varepsilon_{\rm C} = 3\Gamma \; \varepsilon n_{\rm C} R_{\rm C}^3, \tag{15}$$

$$\varepsilon_{\rm L} = \pm\pi|\mathbf{b}|n_{\rm L} R_{\rm L}^2, \tag{16}$$

where the sign in Eq. (16) is chosen in dependence on the interstitial or vacancy nature of dislocation loops.

The use of reliable diffraction parameters related to perfect single-crystalline garnet structure plays a crucible role for the correct quantitative characterization of structural defects by means of the high-resolution double-crystal X-ray diffractometer measurements. The comparison of the theoretical rocking curves calculated according to Eqs. (1)–(5) for perfect YIG and GGG crystals with using the thermal Debye–Waller factors in Fourier components of corresponding crystal polarizabilities determined by powder diffractometry [83] showed very significant discrepancies with the experimental rocking curve measured from YIG
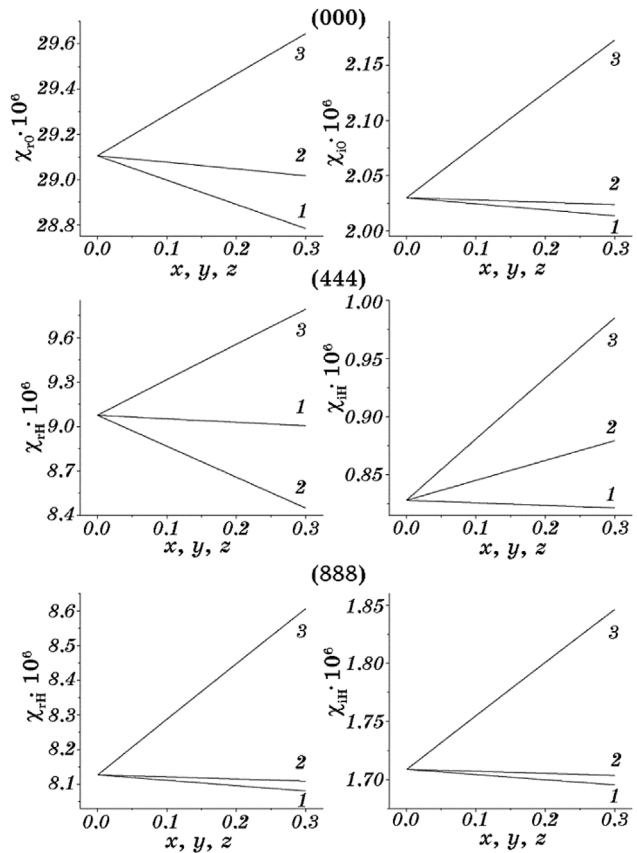

Figure 1 Dependencies of real (left) and imaginary (right) parts of Fourier components of crystal polarizability for YIG 000, 444, and 888 reflections of $CuK\alpha_1$ radiation versus concentrations of Fe^{2+} cations in octahedral positions (x), antisite Fe^{3+} defects (y) and impurity Pb^{2+} cations in dodecahedral positions (z): $1 - y = z = 0$, $2 - x = z = 0$, $3 - x = y = 0$ [82].

film on GGG substrate for the higher order 888 reflection of characteristic $CuK\alpha_1$ radiation (see Fig. 2). These discrepancies between theory and experiment occur too large to be overcome by using any model of crystal imperfections including the thermal atom vibrations and various combinations of point defects and microdefects [82].

Similar difficulties arose also for GGG [84, 85] and NdGG single crystals [86] with respect to 888 reflection of characteristic $CuK\alpha_1$ radiation. For this reason, it was supposed that the most probable cause for the significantly low intensity of calculated rocking curves, as compared with measured ones for the higher order 888 reflection of all the investigated garnet crystals, are the overestimated values of the exponents of thermal Debye–Waller factors. The latter have been found by means of the powder neutron diffractometry and lead to strong decreasing the calculated crystal reflectivities.

Indeed, after using the data for thermal Debye–Waller factor, which have been found in the diffraction experiment with YIG single crystal [87], namely, when the parameter B for Y^{3+}, Fe^{3+}, and O^{2-} ions was taken equal to 0.16, 0.63,
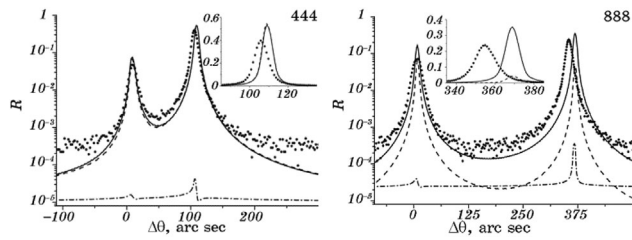
Figure 2 Experimental rocking curves (markers) for 444 and 888 reflections of CuKα$_1$ radiation from YIG film on GGG substrate and theoretical rocking curves calculated for perfect YIG and GGG crystal structures with thermal Debye–Waller factors determined for YIG by using X-ray single crystal [87] and neutron powder [83] diffractometry (solid and dashed lines, respectively). Central parts of peaks from YIG film are shown in insertions; the immediate contribution of thermal diffuse scattering is shown by dash-dotted line [82].

and 2.05 $\overset{\circ}{A}{}^2$, respectively, the theoretical rocking curves for the 888 reflection of perfect YIG crystal become higher and approached to experimental ones [82]. The similar behavior was observed also for the rocking curves measured from the investigated GGG and NdGG single crystals [84–86].

The calculated values of diffraction parameters, namely, Fourier components of the perfect GGG, YIG, and NdGG crystal polarizabilities are given in Table 1. Only with using these values, it was possible to perform the self-consistent treatment of the measured rocking curves for both 444 and 888 reflections (see Fig. 2). Thus, the determination of the characteristics of defects in the investigated YIG film [43] as

Table 1 Fourier components of the polarizability of perfect Gd$_3$Ga$_5$O$_{12}$ (GGG), Y$_3$Fe$_5$O$_{12}$ (YIG), and Nd$_3$Ga$_5$O$_{12}$ (NdGG) garnet crystals for characteristic CuKα$_1$ radiation [82, 84–86].

	$|\chi_{r\mathbf{H}}| \times 10^6$		
hkl	GGG	YIG	NdGG
000	36.342	25.991	36.828
444	12.529	4.710	12.991
888	10.973	1.649	11.768
	$\left|\chi_{i\mathbf{H}}^{\sigma}\right| \times 10^6$		
hkl	GGG	YIG	NdGG
000	3.602	5.448	3.33
444	3.266	1.424	2.995
888	3.424	0.468	3.154
	$\left|\chi_{i\mathbf{H}}^{\pi}\right| \times 10^6$		
hkl	GGG	YIG	NdGG
000	3.602	5.448	3.33
444	2.052	0.894	1.881
888	1.669	0.228	1.538

well as GGG and NdGG single crystals [84–86] was performed by fitting these curves in the whole angular range of measurements (see Section 3).

4.1.3 Diffuse component of the reflectivity of imperfect crystal The "integral" diffuse component of the crystal reflectivity, which is measured by DCD with widely open detector window and represents the differential diffuse scattering intensity integrated over Ewald sphere (over exit angles), can be written for the case of Bragg diffraction geometry in the approximation of semi-infinite crystal as follows [11, 12]:

$$R_{\mathrm{diff}}(\Delta\theta) = F_{\mathrm{dyn}}(\Delta\theta)\mu_{\mathrm{HH}}(\Delta\theta)/(2\gamma_0\mu). \tag{17}$$

Here, the factor $F_{\mathrm{dyn}} \sim 1$ describes the angular modulation of diffuse scattering intensity, which is caused by the dynamical interference of strong Bragg waves. The interference absorption coefficient μ in denominator of Eq. (17) describes the extinction effect for diffusely scattered waves and can be estimated as $\mu(\Delta\theta) \sim \pi/\Lambda$ within the total reflection range and $\mu(\Delta\theta) \approx (1+b)\mu_0/(2\gamma_0)$ outside this range.

The imaginary part of dispersion correction due to diffuse scattering $\mu_{\mathrm{HH}}(\Delta\theta)/K$, which is involved in Eq. (17), can be represented, if the defect concentrations are sufficiently small to satisfy the superposition low for static displacement fields of atoms, as the sum of the coefficients of the absorption due to diffuse scattering for defects of α type with ith size $\mu_{\mathrm{ds}}^{\alpha i}(k_0)$:

$$\mu_{\mathrm{HH}}(\Delta\theta) = \mu_{\mathrm{ds}}(k_0) = \sum_{\alpha}\sum_{i}\mu_{\mathrm{ds}}^{\alpha i}(k_0), \tag{18}$$

where $k_0 = K\Delta\theta \sin 2\theta_{\mathrm{B}}$. The expressions (17) and (18) provide the description of diffuse scattering intensity contributions from several defect types to the measured rocking curves, on the one hand, and the absorption of coherent scattering component due to diffuse scattering, on the other hand (details see in Ref. [12]).

The absorption coefficient due to diffuse scattering from microdefects of only one type, i.e., randomly oriented dislocation loops or spherical amorphous clusters or new phase particles, in Eq. (18) is described by the expression:

$$\mu_{\mathrm{ds}}(k_0) = cC^2E^2m_0J(k_0), \tag{19}$$

$$J(k_0) = \begin{cases} J_{\mathrm{H}}(k_0) + J_{\mathrm{H-SW}}(k_0) + \tilde{J}_{\mathrm{H}}(k_0) & \text{at}\,|k_0| \leq k_{\mathrm{m}}, \\ J_{\mathrm{SW}}(k_0) & \text{at}\,|k_0| \geq k_{\mathrm{m}}. \end{cases} \tag{20}$$

The angular dependence of the "integral" diffuse scattering intensity in the Huang scattering region is described by symmetric (J_{H}, $J_{\mathrm{H-SW}}$) and antisymmetric ($\tilde{J}_{\mathrm{H}}$) components in Eq. (20) as follows:

$$J_{\mathbf{H}}(k_0) = b_2 \ln \frac{k_{\mathrm{m}}^2 + \mu^2}{k_0^2 + \mu^2} + (b_3 k_0^2 + b_4 \mu^2)$$

$$\times \left(\frac{1}{k_{\mathrm{m}}^2 + \mu^2} - \frac{1}{k_0^2 + \mu^2} \right), \qquad (21)$$

$$J_{\mathrm{H-SW}}(k_0) = b_2 - \frac{1}{2} \frac{b_3 k_0^2 + b_4 \mu^2}{k_{\mathrm{m}}^2 + \mu^2}, \qquad (22)$$

$$J_{\mathrm{SW}}(k_0) = \frac{k_{\mathrm{m}}^2 + \mu^2}{k_0^2 + \mu^2} \left(b_2 - \frac{1}{2} \frac{b_3 k_0^2 + b_4 \mu^2}{k_0^2 + \mu^2} \right), \qquad (23)$$

$$\tilde{J}_{\mathbf{H}}(k_0) = b_1 \left(\sqrt{k_{\mathrm{m}}^2 + \mu^2} - \sqrt{k_0^2 + \mu^2} \right), \qquad (24)$$

where c is the defect concentration, k_{m} is the radius of the boundary between Huang and Stokes-Wilson scattering regions, and

$$m_0 = 0.25 \ \pi v_{\mathrm{c}} (H|\chi_{r\mathbf{H}}|/\lambda)^2.$$

The coefficients $b_i (i = \overline{1,4})$ in Eqs. (21)–(24) are connected with characteristics of microdefects by following relationships:

$$b_1 = 4 L_{\mathbf{H}} \sqrt{B_2}/(cH),$$
$$b_2 = B_1 + 0.5 B_2 \cos^2 \theta_{\mathrm{B}},$$
$$b_3 = B_2 (0.5 \cos^2 \theta_{\mathrm{B}} - \sin^2 \theta_{\mathrm{B}}),$$
$$b_4 = B_2 (0.5 \cos^2 \theta_{\mathrm{B}} - \cos^2 \psi), \qquad (25)$$

where ψ is the angle between the crystal surface and reflecting planes.

It should be remarked that in the case of several randomly distributed defect types, the superposition law is supposed to be valid also for the exponent of static Krivoglaz–Debye–Waller factor in Eqs. (6) and (7), similarly to that for the absorption coefficients due to diffuse scattering in Eq. (18).

4.2 Reflectivity of thin film

4.2.1 Coherent component of the reflectivity of imperfect film structures
Epitaxial films are characterized from the structural point of view by the presence of growth defects and inhomogeneous strains in both subsurface and transition layer between film and substrate. These structural peculiarities together with intentional modifications of surfaces and interfaces can significantly influence their physical properties. For example, the surface treatment of the YIG film in Pt/YIG-based devices results in an extraordinary increase in the efficiency of the spin-to-magnon conversion at room temperature [88]. The influence of the substrate induces strong changing of various statical and dynamical properties of the ferroelectric thin film [89]. Both doping ions and the presence of substrate induce a strong changing of the polarization and lead to a shift of the phase transition temperature in antiferroelectric thin films [90], etc.

If the total film thickness is of the order of the extinction length, the fully dynamical consideration is required for the correct interpretation of observed diffraction patterns. The relatively simple analytical description of the dynamical X-ray diffraction in such imperfect inhomogeneous single-crystalline systems can be achieved due to their subdivision into imaginary laminae with randomly distributed defects and constant average strain in each lamina, i.e., by using the so-called layer approximation. Then the recurrence relation between coherent amplitude reflection coefficients of two such imperfect multilayer systems consisting of any number of M and $(M-1)$ layers can be derived from the generalized statistical dynamical theory of X-ray diffraction by imperfect single crystals for the case of arbitrary asymmetrical Bragg diffraction geometry [82]:

$$R_j = \left[r_j + R_{j-1} \left(e_j^{-1} t_j^2 - \zeta_j^{-1} r_j^2 \right) \right] / \left(1 - \zeta_j^{-1} r_j R_{j-1} \right). \qquad (26)$$

Here r_j and t_j are amplitudes reflectivity and transmissivity of jth layer, respectively ($|\zeta_j| \approx 1$):

$$r_j = \sqrt{\zeta_j} \left[y_j + i \sqrt{y_j^2 - 1} \cot \left(A_j \sqrt{y_j^2 - 1} \right) \right]^{-1}, \qquad (27)$$

$$t_j = \sqrt{e_j} \left[\cos \left(A_j \sqrt{y_j^2 - 1} \right) \right.$$
$$\left. - i \left(y_j / \sqrt{y_j^2 - 1} \right) \sin \left(A_j \sqrt{y_j^2 - 1} \right) \right]^{-1}. \qquad (28)$$

The following notation was used: $A_j = \pi d_j / \Lambda_j$ and $\Lambda_j = \lambda (\gamma_0 |\gamma_{\mathbf{H}}|)^{1/2} / \sigma_j$ with d_j being the thickness of jth layer and the index j denoting the relation of corresponding quantities to jth layer.

The amplitude absorption and phase factor in Eq. (28) can be represented as follows:

$$e_j = \exp[-iK(\chi_{0j} + \Delta\chi_{00j}) d_j / \gamma_0 - 2i A_j y_j]. \qquad (29)$$

The normalized angular deviation y_j in Eqs. (27)–(29) is defined by deviations $\Delta\mathbf{H}$ of the reciprocal lattice vector of substrate $\mathbf{H} \equiv \mathbf{H}_0$ ($j = 0$) due to sample rotation and $\Delta\mathbf{H}_j$ of the reciprocal lattice vector $\mathbf{H}_j = \mathbf{H}_0 + \Delta\mathbf{H}_j$ due to strain in jth layer ($j = 1$ to M), respectively:

$$y_j = (\alpha_j - \alpha_{0j}) \sqrt{b} / \sigma_j, \qquad (30)$$

$$\alpha_j = \left(\mathbf{K}_j + \mathbf{H}_j\right)\left(\Delta \mathbf{H} + \Delta \mathbf{H}_j\right)/K_j{}^2$$
$$\approx -(\Delta\theta + \Delta\theta_j)\,\sin(2\theta_{\mathrm{B}}), \tag{31}$$

$$a_{0j} = \frac{1}{2}\left[\chi_{0j} + \Delta\chi_{\mathbf{HH}j} + \frac{1}{b}\left(\chi_{0j} + \Delta\chi_{00j}\right)\right],$$

$$\Delta\theta_j = \left(\varepsilon_\perp^j \cos^2\psi + \varepsilon_\parallel^j \sin^2\psi\right)\,\mathrm{tg}\,\theta_{\mathrm{B}}$$
$$+\,\mathrm{sgn}(1-b)\left(\varepsilon_\perp^j - \varepsilon_\parallel^j\right)\,\sin\psi\,\cos\psi, \tag{32}$$

where $\Delta\theta \approx \Delta H/H$ (with $\Delta\mathbf{H} \perp \mathbf{H}$) is the angular deviation of the substrate from the exact Bragg position due to sample rotation, $\Delta\theta_j$ is the angular deviation of jth layer from the substrate orientation due to strain, $\varepsilon_\perp^j$ and $\varepsilon_\parallel^j$ are normal and parallel strain components in jth layer, and ψ is the angle between the crystal surface and reflecting planes. It should be remarked here yet once that the additional average strain in jth layer can be caused not only by differences in chemical compositions but also due to randomly distributed defects of various types.

Thus, the coherent component of reflectivity for the multilayered crystal system which consists of M layers with randomly distributed defects can be represented in the two-wave approximation at Bragg diffraction geometry as follows:

$$R_{\mathrm{coh}}(\Delta\theta) = |R_{\mathrm{M}}(\Delta\theta)|^2. \tag{33}$$

Here, the amplitude reflectivity of upper Mth layer $R_{\mathrm{M}}(\Delta\theta)$ is determined by using the recurrence relation (26) and by starting the recurrence procedure from the thick substrate reflectivity (see Eq. (1)).

4.2.2 Diffuse component of the reflectivity of imperfect film structures

The diffuse component of the rocking curve, which is measured from the multilayer system with randomly distributed defects by using DCD with widely open detector window, can be represented as follows [82]:

$$R_{\mathrm{diff}}(\Delta\theta) = \sum_{j=0}^{M} F_j^{\mathrm{ext}} F_j^{\mathrm{abs}} R_{\mathrm{diff}}^j(\Delta\theta), \tag{34}$$

where the effects of extinction and absorption are described by corresponding factors F_j^{ext} and F_j^{abs}. The extinction factor in Eq. (34) describes the X-ray intensity redistribution between transmitted and diffracted coherent waves in jth layer:

$$F_0^{\mathrm{ext}} = \left|1 - c_0^\delta\right|^2, \; F_j^{\mathrm{ext}} \approx 1,$$

$$c_j^\delta = (\zeta_j b)^{1/2}\left[y_j + (-1)^\delta \sqrt{y_j{}^2 - 1}\right] j = \overline{1,M}, \tag{35}$$

where the index δ is equal to 1 or 2 in dependence on the sign of $y_{\mathrm{jr}} = \mathrm{Re}\,y_j$ and designates the number of the wave field existing in the substrate or layers. The absorption of transmitted and scattered waves in the layers lying above jth layer is described in Eq. (35) at $j = 0$ to $(M-1)$ by the factor:

$$F_j^{\mathrm{abs}} = \sum_{i=j+1}^{M} \exp(-\mu_i d_i), \; F_M^{\mathrm{abs}} = 1. \tag{36}$$

The diffuse component of the rocking curve (34) is the sum consisted of modulated diffuse components of reflectivities of the substrate ($j=0$) and layers ($j = \overline{1,M}$):

$$R_{\mathrm{diff}}^j(\Delta\theta) = \mu_{\mathrm{ds}}^j(\Delta\theta) p_j(d_j)/\gamma_0, \tag{37}$$

$$p_j(d_j) = \frac{1 - \exp\left(-2\mu_j d_j\right)}{2\mu_j}. \tag{38}$$

The normal absorption coefficient in Eqs. (36) and (38) includes both linear photoelectric absorption coefficient μ_0^j and absorption coefficient due to diffuse scattering in jth layer:

$$\mu_j = \frac{1}{2}\left(\mu_0^j + \mu_{\mathrm{ds}}^j\right)\left(\frac{1}{\gamma_0} + \frac{1}{|\gamma_{\mathbf{H}}|}\right). \tag{39}$$

If the substrate is thick ($\mu_0 d_0 \gg 1$) and layers are thin ($\mu_j d_j \ll 1$, $d_j \ll |\Lambda_j|$), the diffuse reflectivities in Eq. (37) can be represented, respectively, as follows:

$$R_{\mathrm{diff}}^0(\Delta\theta) = \frac{\mu_{\mathrm{ds}}^0(\Delta\theta)}{(1+b)\mu_0^0}, \; R_{\mathrm{diff}}^j(\Delta\theta) = \frac{\mu_{\mathrm{ds}}^j(\Delta\theta) d_j}{\gamma_0}. \tag{40}$$

It should be remarked here also that the absorption coefficients due to diffuse scattering in the above equations are the sums of corresponding coefficients in the case of several defect types distributed randomly in each layer. Similar superposition law is supposed for the exponent of static Krivoglaz–Debye–Waller factor in each layer as well.

4.3 Reflectivity of ion-implanted garnet crystals and films

After ion implantation, the subsurface layer of garnet crystal or film is additionally saturated by primary and secondary radiation defects, which are distributed randomly and inhomogeneously in depth [91]. These defects create the corresponding strain fields, which can be represented as sums of smooth "in average" – inhomogeneous and random components. The depth profiles of these strain fields can be calculated through concentrations of the amorphous clusters formed by displaced matrix atoms in consequence of energy losses of the implanted ions [82].

The existence of two channels of energy losses for the implanted ions should be taken into account in such calculations, namely, one channel created through the excitation of electronic subsystem and second due to elastic nuclear collisions [82, 92–94]. For the electronic channel, the depth profile of cluster concentration can be set as a decreasing tail of Gaussian ($t_0^{el} \leq 0$, $z \geq 0$):

$$n_C^{el}(z) = n_C^{el,max} f_{el}(z), \ f_{el}(z) = \exp[-(z - t_0^{el})^2/\sigma_{el}^2]. \quad (41)$$

For the nuclear channel, the depth profile of cluster concentration can be represented as an asymmetric Gaussian $f_{nucl}(z) = \exp[-(z - t_0^{nucl})^2/\sigma_{nucl}^2]$ ($t_0^{nucl} > 0$, $z \geq 0$):

$$n_C^{nucl}(z) = n_C^{nucl,max} f_{nucl}(z), \quad (42)$$

where $\sigma_{nucl} = \sigma_1$ at $z \leq t_0^{nucl}$, and $\sigma_{nucl} = \sigma_2$ at $z \geq t_0^{nucl}$.

Resulting strain profile in the implanted layer can be calculated as the sum of depth-depended strain profiles created by the two distributions of cluster concentrations along the normal to crystal surface:

$$\varepsilon_\perp(z) = \varepsilon_\perp^{el}(z) + \varepsilon_\perp^{nucl}(z), \quad (43)$$

where the average strain components from the clusters distributed randomly at the depth z in a lamina of dz thickness are calculated by using Eqs. (15), (41), and (42):

$$\varepsilon_\perp^{el}(z) = 3\Gamma \varepsilon n_C^{el}(z) R_C^3,$$

$$\varepsilon_\perp^{nucl}(z) = 3\Gamma \varepsilon n_C^{nucl}(z) R_C^3.$$

It should be emphasized that radius and strength of spherical clusters were supposed to be channel- and depth-independent for reducing the number of fit parameters.

The depth profile of the so-called amorphization factor can be described by the static Krivoglaz–Debye–Waller factor. Namely, the exponent of this factor should be calculated according to Eq. (7) through characteristics of clusters in implanted layer and its dependence on depth will be described by the sum of two distributions of cluster concentrations:

$$n_C(z) = n_C^{el}(z) + n_C^{nucl}(z).$$

The depth dependence of the attenuation of coherent component of diffraction intensity from the implanted layer is described along similar lines. Namely, the coefficient of absorption due to diffuse scattering, μ_{ds}, is calculated through characteristics of clusters in implanted layer by using Eqs. (19)–(24), where $c = n_C(z)/v_c$ should be put.

Thus, for the realization of quantitative X-ray diffraction characterization of the ion-implanted garnet single crystal or garnet film by using the above-described theoretical approach, these imperfect structures can be considered as an inhomogeneous multilayer system in each layer of which the strain consist of average (constant) and fluctuating components. This diffraction model provides physically clear connections between defect characteristics of imperfect structure and diffraction parameters sensitive to crystal structure imperfections. In addition, the self-consistent character of calculation of these parameters should be emphasized, what complements the self-consistency between coherent and diffuse components of diffraction intensity in this model.

5 Defects and strains in imperfect garnets
5.1 Characterization of as-grown garnets
5.1.1 As-grown GGG crystal The most typical point defects in garnet crystals are extrinsic substitutional point defects, intrinsic antisite defects, and vacancies (see, e.g., Refs. [95, 96]). Particularly, the creation of antisite defects in GGG crystals grown by Czochralski method from the melt-solution ($3Gd_2O_3 + 5Ga_2O_3$) occurs due to the gallium evaporation, which causes the change of stoichiometric ratio 3:5 toward the increase of gadolinium cations Gd^{3+}. Then the formation of vacancies of gallium cations Ga^{3+} in octahedral positions and vacancies of oxygen anions O^{2-} is possible from the thermodynamic point of view.

Additionally, as follows from the observations by means of Mössbauer spectroscopy for a number of garnet single crystals, including GGG and YIG crystals, the possibility of an exchange between approximately 10% of the cations placed in dodecahedral and octahedral positions can be regarded as their immanent property [97].

Thus, the general structural formula of the as-grown GGG single crystal with intrinsic substitutional point defects can be written in accordance with the published data as follows:

$$\{Gd_{3-y}Ga_y\}[Ga_{2-x-y-z}Gd_{x+y} \ V_z^{Ga}](Ga_3)O_{12-\delta} \ V_\delta^O, \quad (44)$$
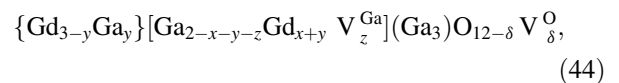
where $\delta = 3z/2$, x and y are concentrations of Gd^{3+} antisite defects in octahedral and Ga^{3+} antisite defects in dodecahedral positions, respectively, the letter V denotes vacancies, z and δ are concentrations of vacancies of Ga^{3+} cations in octahedral positions and vacancies of O^{2-} anions, respectively.

The presence of point defects causes the changes of both structure factors and lattice parameters and, consequently, Fourier components of crystal polarizability. Later influence on the form of coherent component of rocking curve, which changes at typical point defect concentrations, however, are too small to describe completely the measured rocking curves even in their central parts.

The analysis of the immediate contribution of diffuse scattering intensity from various antisite defects and vacancies was performed with using their typical concentrations determined experimentally for GGG crystals namely, $x \approx 0.2$, $y \approx 0.3$, and $z \approx 0.1$ [95, 97]. The

performed calculations have shown that in the measured angular ranges for both 444 and 888 reflections these contributions cannot provide the acceptable fit of the observed rocking curves because of their smallness and wide angular intensity distribution [84, 85]. The analysis of the immediate contribution of thermal diffuse scattering intensity to the measured rocking curves, which was performed with using elastic constants known for GGG single crystals from acoustic measurements [98] and explicit analytical expressions for this intensity [12], has given the results similar to those obtained for point defects.

Consequently, the diffuse scattering intensity contributions from microdefects should be taken into account additionally to both contributions from point defects and thermal atom vibrations. At the same time, the contributions from point defects to the exponent $L_{\mathbf{H}}$ of static Krivoglaz–Debye–Waller factor can be comparable with those from thermal vibrations and, consequently, can substantially influence both coherent and diffuse components of diffraction intensities and cannot be neglected.

Thus, to achieve the good fit being uniform in the whole angular range of rocking curve measurements, including the total reflection range, simultaneously for two reflections (see Fig. 3), it was necessary to suppose, that two microdefect types are present in the as-grown GGG crystal. Namely, both dislocation loops of $(1/2)\langle 111 \rangle$ type [99–102] and spherical clusters of unknown nature (e.g., new phase particles like Gd_2O_3), cf. Refs. [103, 104]) were considered.

The characteristics of spherical clusters and circular dislocation loops, namely, average radius and concentration (see Table 2) were determined independently for two reflections and then matched to achieve sufficiently good mutual agreement. When fitting, the fixed value $\varepsilon = 0.03$ of the misfit strain at the boundary between the cluster and GGG matrix was accepted.

Thus, the good fit quality for both reflections in the whole measured angular range including the total reflection range and far rocking curve tails should be emphasized. This result has been provided due to the self-consistent description of coherent and diffuse X-ray scattering in the imperfect GGG crystal. It should be

Table 2 Average characteristics of microdefects in as-grown GGG crystal [84].

type of microdefects	characteristics of microdefects in GGG		
dislocation loops	radius R_L, nm	100	
	concentration n_L, cm^{-3}	8.0×10^{11}	
clusters	radius R_C, nm	50	10
	concentration n_C, cm^{-3}	5.0×10^{11}	1.0×10^{14}

especially emphasized the unique character of the obtained information on statistical characteristics of small microdefects in nearly perfect GGG crystal, which practically cannot be assessed by direct observation methods for such materials.

5.1.2 As-grown NdGG crystal The most typical point defects in NdGG single crystals are similar to those in GGG crystals. Thus, the general structural formula of the as-grown NdGG single crystal with intrinsic point defects can be written in accordance with the published data as follows:

$$\{Nd_{3-y}Ga_y\}[Ga_{2-x-y-z}Nd_{x+y}V_z^{Ga}](Ga_3)O_{12-\delta}V_\delta^O, \tag{45}$$
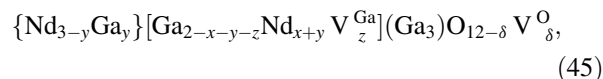
where $\delta = 3z/2$, x and y are concentrations of Nd^{3+} antisite defects in octahedral and Ga^{3+} antisite defects in dodecahedral positions, respectively, the letter V denotes vacancies, z and δ are concentrations of vacancies of Ga^{3+} cations in octahedral positions and vacancies of O^{2-} anions, respectively.

As was observed for the GGG crystal investigated earlier, the presence of point defects in the NdGG single crystal causes similarly too small changes of Fourier components of the crystal polarizability to describe completely the form of central peaks observed on the rocking curves measured for 444 and 888 reflections. In addition, the calculated immediate contributions of the thermal diffuse scattering intensity as well as diffuse scattering intensity from various antisite defects and vacancies, which were determined with using their typical concentrations, cannot provide fitting the observed rocking curves because of their smallness and wide angular intensity distribution.

Thus, again the diffuse scattering intensity contributions from microdefects, namely, dislocation loops of $(1/2)\langle 111 \rangle$ type and spherical clusters of unknown nature (e.g., new phase particles like Nd_2O_3), have been taken into account additionally to both contributions from point defects and thermal atom vibrations. Then the good uniform fit has been achieved simultaneously for two reflections in the whole angular range of rocking curve measurements including the total reflection range (see Fig. 4).
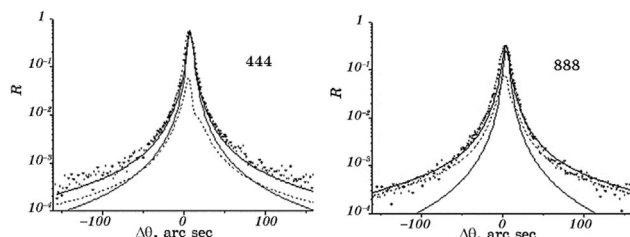

Figure 3 Experimental and theoretical rocking curves (markers and thick solid lines, respectively) for GGG 444 and 888 reflections of CuKα_1 radiation, the thin solid and dashed lines describe coherent component and diffuse scattering intensity contributions from microdefects, respectively [84].
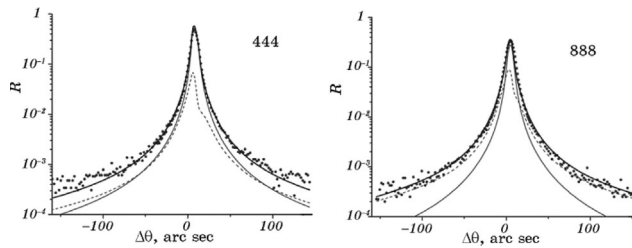
Figure 4 Experimental and theoretical rocking curves (markers and thick solid lines, respectively) for NdGG 444 and 888 reflections of CuKα_1 radiation, the thin solid and dashed lines describe coherent component and diffuse scattering intensity contributions from microdefects, respectively [86].

The characteristics of spherical clusters and circular dislocation loops in the investigated NdGG single crystal (see Table 3) were determined independently by analyzing the measured rocking curves for two reflections and then matched to achieve sufficiently good mutual agreement. When fitting, the fixed value $\varepsilon = 0.03$ of the misfit strain at the boundary between the cluster and NdGG matrix was supposed.

It is remarkable that the values of microdefect characteristics determined for as-grown NdGG crystal are very close to those obtained for as-grown GGG single crystal (*cf.* Tables 2 and 3). This result can be explained by the similar growth conditions of both GGG and NdGG single crystals, which have identical crystallographic structure, as well as the similar thermodynamic and mechanical properties of these two garnet structures, which predetermine the type and formation character of growing nanoclusters and microdefects.

## 5.2 Characterization of defects in as-grown thin YIG film

In YIG films, similarly to GGG and NdGG crystals, the presence of various antisite defects and vacancies has been established by spectroscopic and chemical methods [105–108]. The creation of O^{2-} anion vacancies has been shown to be energetically favorable at the charge compensation due to partial recharging from Fe^{3+} to Fe^{2+} cations in octahedral positions [109–111]. In addition, the possibility of exchanging between the cations placed in dodecahedral and octahedral positions of YIG

Table 3 Average characteristics of microdefects in as-grown NdGG crystal [86].

type of microdefects	characteristics of microdefects in NdGG		
dislocation loops	radius R_L, nm	100	
	concentration n_L, cm^{-3}	8.0×10^{11}	
clusters	radius R_C, nm	50	10
	concentration n_C, cm^{-3}	5.0×10^{11}	5.0×10^{13}

structure should be taken into account [97]. Among impurity point defects, the most essential influence on structure characteristics and physical properties of YIG films have Pb^{2+} cations which can substitute Y^{3+} cations in dodecahedral positions with corresponding charge compensation at the cost of O^{2-} anion vacancies [112, 113].

Thus, the general structural formula of the as-grown YIG film with intrinsic and impurity point defects can be written in accordance with the published data as follows:

$$\{Y_{3-y-z}^{3+}Fe_y^{3+}Pb_z^{2+}\}[Fe_{2-x-y}^{3+}Fe_x^{2+}Y_y^{3+}](Fe_3^{3+})O_{12-\delta}V_{\delta}^O,$$

(46)
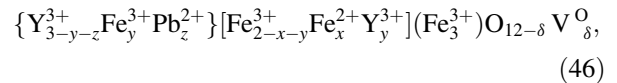
where $\delta = (x+z)/2$, x is the concentration of partially dissociated Fe^{2+} cations in octahedral positions, y is the concentration of Y^{3+} antisite defects in octahedral and Fe^{3+} antisite defects in dodecahedral positions, respectively, z is the concentration of Pb^{2+} impurity cations in dodecahedral positions.

Similarly to GGG and NdGG crystals, the various growth microdefects, including new phase particles like Fe_2O_3, Y_2O_3, or $YFeO_3$, and dislocation loops of (1/2) $\langle 111 \rangle$ type are expected to be always present in YIG films additionally to point defects [114–118]. Besides, the inhomogeneous strained transition layer between film and substrate due to lattice mismatch as well as near the film surface due to uncontrollable entering impurity atoms at initial and final stages of the film growth can be formed [119].

Thus, to analyze the measured rocking curves, the investigated single-crystalline YIG film on GGG substrate was considered as an imperfect multilayer system. This system was supposed to consist, in both film and substrate, of a number of laminae with constant strain in each of them and with additional fluctuating strain fields from randomly distributed defects.

First of all, the immediate contributions to the measured rocking curves, which are given by diffuse scattering intensity from various antisite defects and vacancies, were analyzed with using their typical concentrations determined experimentally for YIG crystals [97, 105] (see Fig. 2). In addition, the contribution of the thermal diffuse scattering intensity was calculated according to the diffraction model proposed in Ref. [12] and with using the elastic constants known for YIG single crystals from acoustic measurements [120]. The performed calculations have shown that in the measured angular ranges for both 444 and 888 reflections these contributions cannot provide the acceptable fit of the observed rocking curves because of their smallness and wide distribution. Nevertheless, at this stage it was possible to refine the concentrations of intrinsic and extrinsic point defects due to matching the positions of diffraction peaks observed from film and substrate, which are very sensitive to these characteristics (*cf.* Figs. 2 and 5).

As consequence, it was established that the additional angular shifts of diffraction peaks by nearly 2 and 6 arcsec
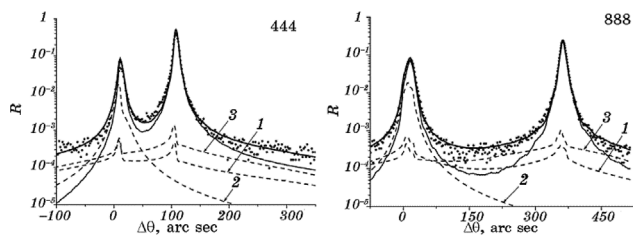
Figure 5 Experimental and theoretical rocking curves (markers and thick solid lines, respectively) for YIG 444 and 888 reflections of CuKα₁ radiation, the thin solid and numbered dashed lines describe coherent component and diffuse scattering intensity contributions from small (*1*) and large (*2*) dislocation loops, and clusters (*3*), respectively [82].

for 444 and 888 reflections, respectively, were caused by the concentration of Pb^{2+} impurity cations in dodecahedral positions, which was estimated to be $z \approx 0.001$. It should be remarked also that the concentrations of intrinsic point defects ($x \approx 0.001$, $y \approx 0.001$) were refined at next fit stages due to account for their contributions to the exponent of static Krivoglaz–Debye–Waller factor with the simultaneous conservation of the distance between diffraction peak positions.

At the next step, the measured rocking curves were fitted under the supposition that also dislocation loops of $(1/2)\langle 111 \rangle$ type are present in the YIG film additionally to point defects. Again, this fit step was not sufficiently satisfactory because of the "saturation effect." Namely, at the proper choice of dislocation loop radii (see Table 4), which provides the correct description for observed halfwidth of rocking curve and decrease law at far tails for both 444 and 888 reflections, the required increase of the dislocation loop concentration led to significant rising the exponent of the static Krivoglaz–Debye–Waller factor. The correspondingly decreased factor strongly suppressed both coherent and diffuse intensity components.

For this reason, the characteristics of randomly distributed spherical clusters (e.g., inclusions of $YFeO_3$, Fe_2O_3, or Fe_3O_4 new phase particles [114, 115]) were additionally included into the fit procedure. The strain at the boundary between inclusions and YIG matrix was held at the fixed value $\varepsilon = 0.03$. Then inclusion and dislocation loop characteristics were determined independently for each of two reflections and subsequently matched to achieve sufficiently good mutual agreement (see Table 4). Additionally, also the characteristics of Gd_2O_3 inclusions and

dislocation loops in GGG substrate were refined with using their values determined previously [84, 85] as starting ones to achieve an overall good fit quality in the whole measured angular ranges for both 444 and 888 reflections (see Fig. 5).

Up to this point, the misfit strain profile at the boundary between film and substrate was supposed to be sharp. Probably because of this simplification the clearly visible discrepancies remained between the forms of theoretical and experimental rocking curves at the both peak tops for two reflections. After choosing the strain profile at both sides of the boundary between film and substrate as shown in Fig. 6 these discrepancies have been removed.

Moreover, it was possible to improve additionally the fit quality at the right tail of rocking curve for the 444 reflection (see Fig. 7) due to setting the small strain in the thin film surface layer with nearly 20 nm thickness (see insertion in Fig. 6). It should be remarked that the formation of such surface layers in YIG films due to cation redistribution was observed in spectroscopic and Rutherford backscattering measurements [119].

Thus, the careful accounting for both existing sets of randomly distributed point defects and microdefects as well as inhomogeneous strain fields has provided the good fit quality of the measured rocking curves simultaneously for both 444 and 888 reflections in the whole angular range including the total reflection ranges of both YIG film and GGG substrate. Yet once it should be emphasized that this result been achieved due to the self-consistent description of coherent and diffuse scattering connected with defect characteristics via mutually consistent explicit analytical relations.

5.3 Characterization of defects in ion-implanted garnet crystals and films

5.3.1 GGG crystal implanted with F⁺ ions The model of defect structure in the implanted GGG crystals included two types of randomly distributed grown-in microdefects, namely, spherical clusters and circular prismatic dislocation loops as well as secondary radiation defects in form of spherical amorphous clusters distributed inhomogeneously in depth [121]. The implanted GGG crystals in whole were considered as multilayer systems in each layer of which the strain was consisted of average and fluctuating components.

The depth profiles of the average strain caused by ion implantation were calculated through concentrations of the spherical amorphous clusters formed by displaced matrix

Table 4 Average characteristics of microdefects in the YIG film grown on GGG substrate [82].

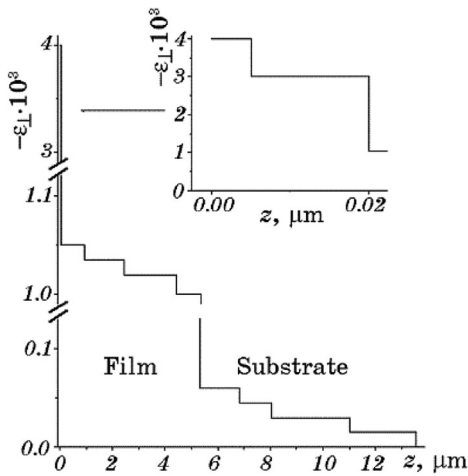| type of microdefects	characteristics of microdefects	GGG substrate		YIG film
dislocation loops	radius R_L, nm	90	5	5
	concentration n_L, cm⁻³	1.2×10^{12}	1.0×10^{15}	1.0×10^{15}
spherical clusters	radius R_C, nm	8		10
	concentration n_C, cm⁻³	1.0×10^{14}		1.0×10^{14}

Figure 6 Strain profiles in YIG film and GGG substrate [82].

atoms in consequence of energy losses of the implanted ions through excitation of electronic subsystem and elastic nuclear collisions. Resulting strain profile in implanted layer was calculated as the sum of depth-depended strain profiles created by the two distributions of cluster concentrations along the normal to crystal surface.

The fit of the measured rocking curves (Fig. 8) was performed by using the theoretical approach described above in Section 3 and with carrying out the convolution of theoretical rocking curves with DCD resolution function. The existence of two channels of energy losses for the implanted light ions, namely, through elastic nuclear collisions and inelastic electronic excitations, was taken into account (Fig. 9). Both these channels were supposed to be the origin of formation of spherical amorphous clusters in the implanted layer. Such characteristics of clusters in implanted layer as radius and strain at the boundary with crystal matrix were supposed to be equal for both channels. The cluster radii have been determined to be approximately 1.7 nm at the value of volume strain between cluster and crystal matrix supposed to be equal $\varepsilon = 0.03$. The
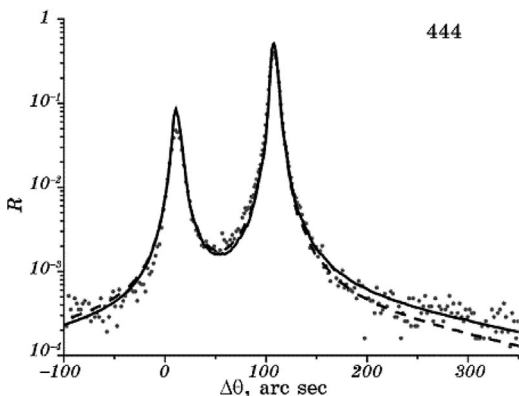

Figure 8 Measured and calculated (solid line) rocking curves for 444 reflection of CuKα_1 radiation from GGG crystals implanted with F$^+$ ions of energy $E = 90$ keV at doses $D = 10^{13}$ (top row) and 40×10^{13} cm^{-2} (bottom row). Coherent and diffuse rocking curve components are shown by dashed and dot-dashed lines, respectively [121].

corresponding maximal values of cluster concentrations and strains found at various implantation doses are given in Table 5.

It should be remarked that the strain profile parameters connected with nuclear and electronic energy loss channels have been determined to be the same at all the applied implantation doses and equal to $t_0^{nucl} = 85$ nm, $\sigma_1 = 80$ nm, $\sigma_2 = 25$ nm, and $t_0^{el} = -75$ nm, respectively. Some variations have been found only for one of two parameters characterizing the strain profile due to electronic energy loss channel, namely, σ_{el}, which values were found to be between 120 and 210 nm at various implantation doses.

The simulation calculations of depth distributions of displaced atoms and implanted F$^+$ ions, which have been performed by using the SRIM-2008 software based on a Monte Carlo method [122], have showed that the penetration depth of displaced atoms (Fig. 9b) practically coincides with the occurrence depth for clusters in implanted layer determined in the diffraction measurements (Fig. 9a). Also, the form of strain profiles for GGG crystals

Figure 7 Experimental (markers) and theoretical rocking curve with and without account of the strain in surface layer (solid and dashed lines, respectively) [82].
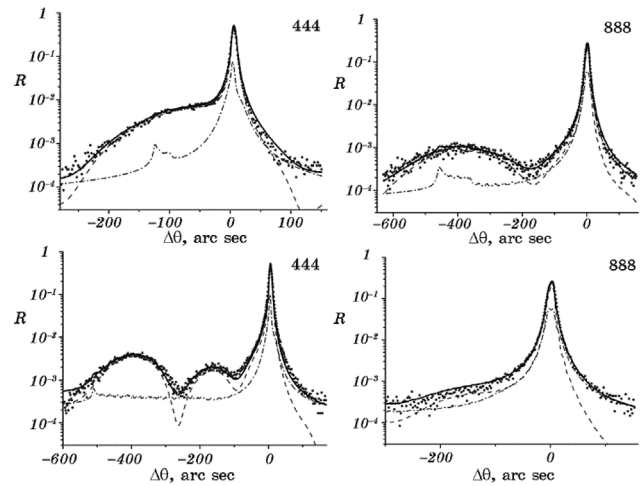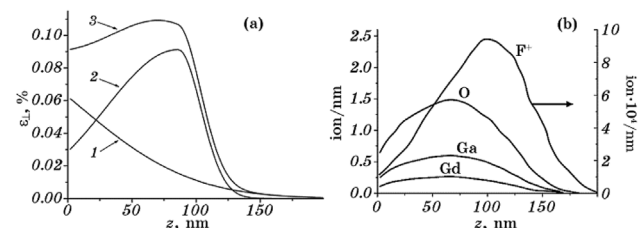

Figure 9 (a) Determined strain profiles in GGG crystal due to electronic (1), nuclear (2), and total (3) energy losses of implanted 90 keV F$^+$ ions at dose 8×10^{12} cm^{-2} [121]. (b) Simulated depth distributions of displaced atoms and implanted F$^+$ ions, normalized to implantation dose.

Original

Paper

Phys. Status Solidi B (2017)   (15 of 22) 1600689

Table 5 Maximal values of cluster concentrations and strains in GGG crystals implanted with 90 keV F^+ ions at various implantation doses [121].

D, cm^{-2}	8×10^{12}	10^{13}	2×10^{13}	4×10^{13}	6×10^{13}
$n_C^{nucl,max}$, cm^{-3}	1.0×10^{19}	1.1×10^{19}	2.6×10^{19}	5.2×10^{19}	16.0×10^{19}
$n_C^{el,max}$, cm^{-3}	1.0×10^{19}	1.0×10^{19}	1.0×10^{19}	1.0×10^{19}	5.5×10^{19}
$\varepsilon_\perp^{nucl,max}$, %	0.09	0.10	0.23	0.46	0.63
$\varepsilon_\perp^{el,max}$, %	0.06	0.07	0.075	0.08	0.18

implanted with 90 keV F^+ ions is close to that of the simulated depth distributions of displaced atoms.

It should be noted the role played by the account for the influence, which is caused by diffuse scattering effects from dislocation loops and clusters in crystal bulk, on both the form of diffraction peaks and rocking curve tails. Namely, this account has allowed for the correct description of X-ray intensity diffracted from the implanted layer and, as consequence, for the quantitative determination of characteristics of both as-grown and secondary radiation defects (see Tables 5 and 6).

In addition, the possibility was provided to avoid systematical errors when determining strain distribution parameters in the implanted layer and elastically relaxed transition layer between crystal bulk and implanted layer (see Fig. 10).

Thus, the quantitative X-ray diffraction characterization of the ion-implanted garnet single crystal has been performed owing to the use of the dynamical diffraction model, which provides physically clear and explicit connections between defect characteristics of imperfect crystal structures and structurally sensitive diffraction parameters. Also, the importance of the self-consistent character of connections between these parameters and defect characteristics, on the one hand, and coherent and diffuse components of diffraction intensity, on the other hand, should be emphasized.

5.3.2 YIG film implanted with F^+ ions The presence of two types of microdefects, namely, spherical clusters and circular prismatic dislocation loops was supposed in the model of defect structure of the implanted epitaxial single-crystalline system of YIG films grown on GGG substrate at fitting the measured rocking curves (Fig. 11) [123]. The influence of point defects (antisite defects and anion vacancies) and thermal diffuse scattering was

taken into account as well. The implanted YIG film on GGG substrate in whole was considered as a multilayer system in each layer of which the strain was consisted of average and fluctuating components. The change of YIG and GGG cubic lattice constants due to point defects was calculated according to empiric analytical expression through concentrations of these defects and effective radii of cations.

When modeling the strain distribution, the implanted layer was subdivided into 2 nm thick laminae, whereas the rest of film and substrate volume was subdivided into layers with thicknesses of the order of few hundreds of nanometers. The depth profiles of the strain caused by ion implantation were calculated through concentrations of the amorphous clusters formed by displaced matrix atoms in consequence of energy losses of the implanted ions.

The existence of two channels of energy losses for the implanted light ions, namely, through excitation of electronic subsystem and elastic nuclear collisions, was taken into account. It was supposed that because of both electronic and nuclear energy losses of implanted ions the spherical amorphous clusters were formed in the implanted layer. Their radii have been determined to be equal approximately 1.7 nm at the fixed value of volume strain between cluster and crystal matrix put to be equal $\varepsilon = 0.03$. The corresponding cluster concentrations found at various implantation doses are given in Table 7.

Such characteristics of clusters in implanted layer as radius and strain at the boundary between cluster and crystal matrix were supposed to be equal for both channels. Resulting strain profile in implanted layer was calculated as the sum of depth-depended strain profiles created by the two distributions of cluster concentrations along the normal to crystal surface (see Fig. 12a).

The rest of strain profile parameters for YIG films implanted with F^+ ions, which are not given in Table 7, have been determined to be equal at all the used

Table 6 Characteristics of grown-in microdefects in GGG crystal implanted with 90 keV F^+ ions [121].

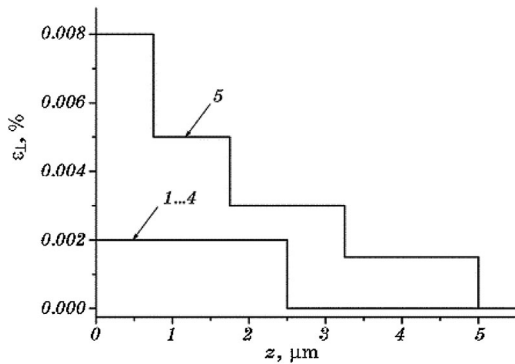| type of microdefects	characteristics of grown-in microdefects	GGG bulk	implanted layer	
dislocation loops	radius R_L, nm	100	100	
	concentration n_L, cm^{-3}	8×10^{11}	1×10^{11}	
clusters	radius R_C, nm	50	50	10
	concentration n_C, cm^{-3}	3×10^{11}	1×10^{11}	1×10^{14}

Figure 10 Additional components of strain profiles in subsurface GGG layer implanted with 90 keV F^+ ions at doses $D = 8 \times 10^{12}$ (1), 10^{13} (2), 2×10^{13} (3), 4×10^{13} (4), 6×10^{13} (5) cm^{-2} [121].

Table 7 Maximal values of cluster concentrations and strains in YIG film implanted with 90 keV F^+ ions [123].

D, cm^{-2}	10^{13}	6×10^{13}	2×10^{14}
$n_C^{nucl,max}$, cm^{-3}	1.1×10^{19}	6.0×10^{19}	2.0×10^{20}
$n_C^{el,max}$, cm^{-3}	1.1×10^{19}	6.0×10^{19}	2.0×10^{20}
$\varepsilon_\perp^{nucl,max}$, $\%$	0.10	0.54	1.79
$\varepsilon_\perp^{el,max}$, $\%$	0.04	0.22	0.73

implantation doses, namely, $t_0^{nucl} = 85$ nm, $\sigma_1 = 80$ nm, $\sigma_2 = 35$ nm, $t_0^{el} = -75$ nm, and $\sigma_{el} = 80$ nm. Only the difference in strain profile parameters for YIG and GGG crystals was that the forward front of the strain profile in GGG crystal was steeper than in YIG film (parameter $\sigma_2 = 25$ nm instead of 35 nm).

It is interesting that the determined depth of strain maximum for F^+ ions implanted in these films occurred unexpectedly the same as that for F^+ ions implanted in GGG crystals (see Section 3.3.1) which mass density (7.094 g cm^{-3}) is remarkably larger than that of GGG crystals (5.17 g cm^{-3}) and for which the stopping range could expected to be correspondingly shorter. This observation may be explained by possible channeling effects for knocked-out matrix atoms (see, e.g., Refs. [124, 125].

It should be noted also that for YIG film implanted with F^+ ions also the relative contribution of the inelastic energy loss channel due to electronic excitations versus the contribution of the elastic energy loss channel due to nuclear collisions was comparable with similar ratio occurred for GGG crystals implanted with F^+ ions of the same energy (cf. Figs. 9 and 12).

The strain profiles for YIG films implanted with 90 keV F^+ ions have been also determined from the simulation calculations using the SRIM-2008 software [126]. These simulations have showed that both the form and depth of strain profiles were close to those determined in the described X-ray diffraction measurements (see also simulated depth distributions of displaced atoms and implanted F^+ ions in Fig. 12b). At the same time, the observed discrepancies in some profile parameters, particularly, in the values of strain profile maxima found in two independent ways can be used to refine and improve the various procedures for simulating the creation of primary and secondary radiation defects (see, e.g., Refs. [127–130]).

The depth profile of the so-called amorphization factor was described by only the static Krivoglaz–Debye–Waller factor, which exponent was calculated by using characteristics of clusters in implanted layer with depth-dependent concentration (see Fig. 13):

$$L_{\mathbf{H}}(z) = L_{\mathbf{H}}^{el}(z) + L_{\mathbf{H}}^{nucl}(z).$$

Additionally, the attenuation of coherent component of diffraction intensity from the implanted layer was described by the coefficient of absorption due to diffuse scattering, μ_{ds}^j, which was calculated similarly through characteristics of clusters in implanted layer (Fig. 13):

$$\mu_{ds}(\Delta\theta, z) = \mu_{ds}^{el}(\Delta\theta, z) + \mu_{ds}^{nucl}(\Delta\theta, z).$$
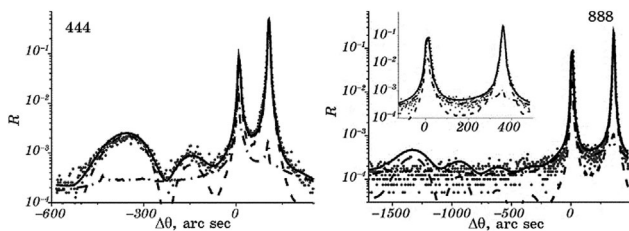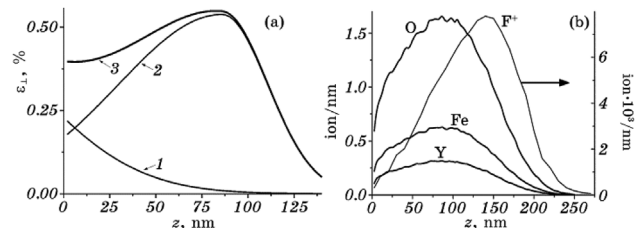

Figure 11 Measured and calculated (solid line) rocking curves for 444 and 888 reflections of $CuK\alpha_1$ radiation from YIG/GGG film system implanted with F^+ ions of energy $E = 90$ keV at dose $D = 6 \times 10^{13}$ cm^{-2}. Coherent and diffuse components of rocking curves are shown by dashed and dot-dashed lines, respectively [123].

Figure 12 (a) Determined strain profiles in YIG film due to electronic (1), nuclear (2), and total (3) energy losses of implanted 90 keV F^+ ions at dose 6×10^{13} cm^{-2} [123]. (b) Simulated depth distributions of displaced atoms and implanted F^+ ions, normalized to implantation dose.
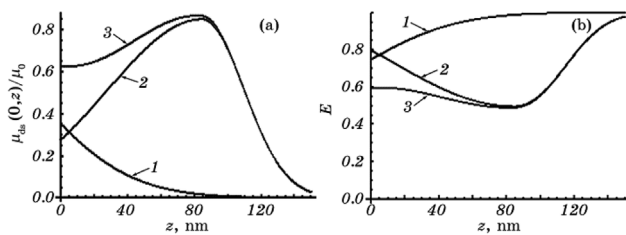
Figure 13 Thickness dependences of the normalized coefficient of absorption due to diffuse scattering (a) and static Krivoglaz–Debye–Waller factor $E = \exp(-L_\mathbf{H})$ (b), which correspond to electronic (*1*), nuclear (*2*), and total (*3*) energy loss channels of F^+ ions implanted in YIG film ($E = 90\,keV$, $D = 2 \times 10^{14}\,cm^{-2}$) for 888 reflection of $CuK\alpha_1$ radiation.

In this way, the physically clear connection between defect characteristics of imperfect structure of the implanted YIG film and structurally sensitive diffraction parameters was provided with minimized number of fit parameters.

The rocking curves measured from an inhomogeneous crystal system like the implanted YIG film on GGG substrate are formed by a superposition of angular distributions of coherent and diffuse scattering intensities from substrate, film, and implanted layer. Such superposition complicates the analysis of the rocking curves for the assessment of strain and amorphization parameters in the implanted layer since the numerous additional fit parameters arise, which characterize defect structure of film and substrate. Nevertheless, the self-consistent character of calculation of all the diffraction parameters simultaneously for two reflections as well as the self-consistency between expressions for coherent and diffuse components of diffraction intensity in the present diffraction model make it possible the determination of the complete set of defect characteristics and strain parameters of the implanted layers in YIG films on GGG substrates.

Moreover, the account for influence of diffuse scattering effects from dislocation loops and clusters in film and substrate on the form of diffraction peaks and tails has allowed for the determination of as-grown defect characteristics, which nearly coincide with those found for as-grown YIG film on GGG substrate (see Section 5.2, Table 4). Simultaneously, the correct description of X-ray intensity diffracted from the implanted layer was possible with avoiding systematic errors due to contributions from diffuse scattering intensity distributions. Additionally, the strain distribution in the transition layer between film and substrate has been determined, which thickness approaches some hundreds of nanometers. It should also be emphasized, that the values of the parameters, which define the form of strain profile, have been determined to be the same for all the implantation doses and both reflections measured.

5.3.3 YIG film implanted with Si^+ ions

The rocking curves measured from the investigated ion-implanted YIG films (Fig. 14) were analyzed by using the above-described dynamical method of high-resolution X-ray diffraction characterization for imperfect compound single crystals with complicated defect structures (Section 4). This method allows for the quantitative characterization of several microdefect types present in the crystal simultaneously and provides the self-consistent determination of statistical microdefect characteristics, i.e., not only average microdefect sizes (from few of micrometers down to tens of nanometers), but also their concentrations and strengths.

At fitting the measured rocking curves, the two types of microdefects, namely, spherical clusters and circular prismatic dislocation loops, were supposed to be present in both YIG film and GGG substrate. The contributions of diffuse scattering from point defects and thermal diffuse scattering were taken into account. The characteristics of microdefects have been found to be the same as given in Table 4 with only the distinction that the nature of spherical clusters in YIG film was specified as presumably new phase γ-Fe_2O_3 particles with strain parameter $\varepsilon \approx -0.08$ and the radius of these particles was correspondingly increased to 10 nm.

Again the implanted YIG film on GGG substrate in whole was considered as a multilayer system in each layer of which the strain was consisted of average and fluctuating components. The existence of two channels of energy losses due to of electronic excitations and nuclear collisions was taken into account for the implanted ions as well. The depth profiles of the strain caused by ion implantation were calculated through concentrations of the spherical amorphous clusters formed by displaced matrix atoms in consequence of energy losses of the implanted ions. The cluster radii have been determined to be approximately 1.5 nm at the value of volume strain between cluster and crystal matrix $\varepsilon = 0.03$. The corresponding cluster concentrations found at various implantation doses are given in Table 8.

The strain profiles determined for YIG film implanted with Si^+ ions are shown in Figs. 15 and 16. The parameters $t_0^{nucl} = 55\,nm$, $\sigma_1 = 45\,nm$, $\sigma_2 = 15\,nm$, $t_0^{el} = -75\,nm$, and
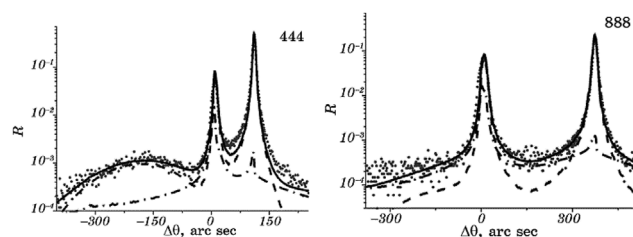

Figure 14 Measured and calculated (solid line) rocking curves for 444 and 888 reflections of $CuK\alpha_1$ radiation from YIG/GGG film system implanted with 90 keV Si^+ ions at the implantation dose $D = 6 \times 10^{13}\,cm^{-2}$. Coherent and diffuse components of rocking curves are shown by dashed and dot-dashed lines, respectively [131].

Table 8 Maximal values of cluster concentrations and strains in YIG films implanted with 90 keV Si^+ ions at various implantation doses [131].

D, cm^{-2}	10^{13}	6×10^{13}	2×10^{14}
$n_C^{nucl,max}$, cm^{-3}	2.0×10^{19}	7.0×10^{19}	20×10^{19}
$n_C^{el,max}$, cm^{-3}	2.0×10^{19}	7.0×10^{19}	20×10^{19}
$\varepsilon_\perp^{nucl,max}$, %	0.12	0.43	1.23
$\varepsilon_\perp^{el,max}$, %	0.01	0.04	0.12

Figure 16 (a) Strain profiles in YIG film implanted with 90 keV Si^+ ions at doses $D = 10^{13}$ (1), 6×10^{13} (2), and $2 \times 10^{14}\,cm^{-2}$ (3), respectively. (b) Strain profile in transition layer between film and substrate [131].

$\sigma_{el} = 50$ nm, which define the form of these strain profiles were put equal at all the used implantation doses for both reflections measured.

The comparison of the depth distributions of displaced atoms (Fig. 15b), which have been calculated by using the SRIM-2008 software, have showed that their form and penetration depth are close to those for clusters in implanted layer determined from the diffraction measurements (Fig. 15a).

It should be noted that for Si^+ ions implanted in YIG film the contribution of the inelastic energy loss channel due to electronic excitations occurred expectedly smaller than the contribution of the elastic energy loss channel due to nuclear collisions as compared with similar ratio for implanted light F^+ ions (cf. Figs. 12 and 15). This observation is supported by the simulation calculations using SRIM-2008 program [132], which showed that also the form of simulated strain profiles is very close to that determined in the diffraction measurements.

6 Discussion The above-described examples of the characterization of structural defects and strain profiles in the as-grown and ion-implanted garnet single crystals and yttrium iron garnet films by using the rocking curves, which have been measured by high-resolution double-crystal X-ray diffractometer with widely open detector window, show some remarkable features.

First of all, the higher sensitivity of this technique to nanometer-sized defects should be emphasized as compared with other ones, in particular, the high-resolution triple-crystal X-ray diffractometer measurements, for which such
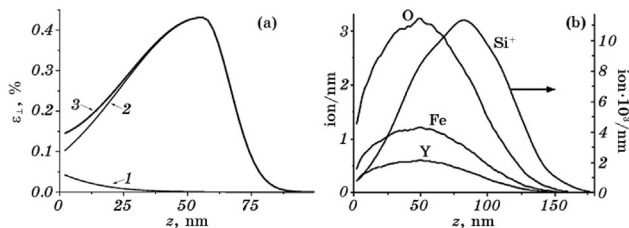

Figure 15 (a) Determined strain profiles in YIG film due to electronic (1), nuclear (2), and total (3) energy losses of implanted 90 keV Si^+ ions at dose $6 \times 10^{13}\,cm^{-2}$ [131]. (b) Simulated depth distributions of displaced atoms and implanted Si^+ ions, normalized to implantation dose.
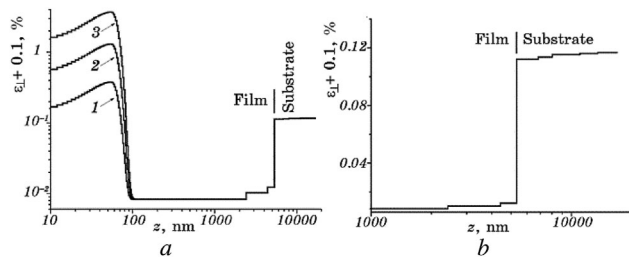
defects with relatively low concentration are almost "invisible" because of small "in-average" distortions created in crystal matrix (cf. Refs. [133–135]). This advantage arises due to the integration of differential diffuse X-ray scattering intensity over two exit angles, i.e., over vertical and horizontal divergences, which increases the contribution of this intensity as compared with coherent one. In consequence, it becomes possible to reveal low concentrations of small growth defects such as clusters and dislocation loops, which sizes are ranged from tens up to hundreds of nanometers in various nearly perfect garnet crystals.

It should be remarked here, that despite this integration, the measured one-dimensional mix of the coherent and diffuse scattering intensity depends on incidence angle and, consequently, the sensitivity of diffuse intensity component to size, strength, and concentration of defects is remained due to different angular dependencies of coherent and diffuse intensity components. That means that a loss of information, as compared with reciprocal space mapping, is only partial, mainly on the symmetry of displacement fields from defects.

On the other hand, the self-consistent description of the dynamical diffraction effects in coherent and partially integrated diffuse scattering intensity distributions within the whole angular range, including the total reflection range, allows for increasing the sensitivity to defects and reliability of defect characterization. Additional important feature of the simultaneous description of the coherent and diffuse intensity components is the possibility to determine the absolute defect concentration values as they predetermine the ratio of these components.

The peculiarity of the investigations described above in Section 5 is that the diffraction pattern observed, e.g., for ion-implanted YIG films, is formed by the superposition of coherent waves scattered from substrate, film, and ion-implanted layer, and consists of their interference with addition of the diffuse scattering intensity from defects in these three regions. As consequence, the dynamical effects appear in both coherent and diffuse scattering intensities since film and substrate are sufficiently thick to cause multiple scattering effects. Moreover, because of the

summation of coherent and diffuse components, the separate analysis of their superimposed contributions is impossible.

Thus, the main advantages of the dynamical theory developed for X-ray diffraction by the ion-implanted imperfect single crystal, multilayer, or film crystal structures containing randomly and inhomogeneously distributed defects are following:

(i) the account for dynamical effects in diffuse scattering from defects in both the substrate and relatively thick film;

(ii) the possibility to analytically treat, simultaneously and self-consistently, both coherent and diffuse component distributions within the whole measured angular range including the total reflection ranges of both substrate and film;

(iii) the absence of necessity to control criteria of the applicability of the formulas from kinematical theory to coherent and/or diffuse scattering intensity components from different crystal regions.

As consequence, the proposed dynamical description of coherent and diffuse scattering intensities provides the significant increase of the accuracy and reliability of the strain and defect characterization without any restrictions imposed on distorted layer thickness or measured angular ranges, which are required to perform the kinematical consideration.

At the same time, for the full determination of the defect characteristics and strain distributions in such kind crystal structures always important are observations at both atomic and micrometer levels. Whereas first ones with atomic resolution provide highly valuable information on the nature of defects and their individual characteristics, the second ones allow for determining the statistical characteristics of defects in the large crystal volumes as well as average strain variations. Just such comprehensive knowledge is usually necessary to assess and control the physical properties of crystal structures of interest.

Of course, when crystal distortions due to defects are sufficiently strong to cause observable diffuse scattering intensities, the measurement of reciprocal space maps by using the high-resolution triple-crystal X-ray diffractometer is of exceptional importance for the assessment of more details on defect structures in ion-implanted layers [136–-138]. However, in general, to understand the mechanisms of growth defects appearance and damage formation in materials irradiated with energetic ions the various additional analytical techniques are necessary, such as transmission electron microscopy, ion and electron Rutherford backscattering spectrometry, Raman spectroscopy, X-ray photoelectron spectroscopy, small-angle X-ray scattering, positron annihilation spectroscopy etc. [52–59, 75, 139–143]. Applications of these techniques provide the unique possibilities to study radiation effects in wide range of implantation depths and gain the information, complementary to X-ray diffraction investigations, on defect configurations and their phase composition, as well as amorphization and recrystallization processes in ion-implanted layers.

Thus, we can conclude that the obtained results show the new possibilities offered by the proposed theoretical method for the treatment of high-resolution double-crystal X-ray diffraction measurements, which allows for improving the quantitative characterization of structural imperfections in real crystal structures with a complicated base and inhomogeneous strain fields.

7 Conclusions The generalized statistical dynamical theory of X-ray diffraction by the imperfect single crystals containing randomly distributed structural defects has been extended to the case of real single crystals and single-crystalline films with complex basis and inhomogeneous strain fields. The developed theoretical diffraction model accounts for the presence of randomly distributed point defects and microdefects of various types as well as the existence of arbitrary inhomogeneous one-dimensional strain fields, in particular, with sharp profiles, i.e., with large strain gradients. The proposed model allows for the self-consistent description of coherent and diffuse components of diffraction patterns measured from such crystal structures due to using the direct explicit analytical relationships between coherent and diffuse scattering amplitudes and statistical characteristics of defects.

Some examples of the application of the developed theoretical model to characterize structural defects and strain profiles in the as-grown and ion-implanted garnet single crystals and YIG films by using the high-resolution double-crystal X-ray diffractometer measurements have been reviewed. The described quantitative characterization of defects and strains has been performed by a combined analysis of the measured rocking curves for two reflections with using the explicit analytical formulas. It should be especially emphasized the unique character of the obtained information on statistical characteristics of point defect clusters and small microdefects in nearly perfect garnet crystals and films, both as-grown and ion-implanted ones, which is not available by using any another of known characterization methods.

The obtained results demonstrate the high information possibilities of the proposed method of the high-resolution double-crystal X-ray diffraction measurements for the quantitative characterization of structural imperfections in real single crystals and single-crystalline film structures with a complicated base and inhomogeneous strain fields. It is worth mentioning that the described method is applicable also to imperfect multilayer crystal structures with arbitrary layer compositions and total multilayer thickness.

References

[1] R. I. Barabash, G. E. Ice, and P. E. A. Turchi (eds.), Diffuse Scattering and the Fundamental Properties of Materials (Momentum Press, New Jersey, 2009), p. 444.

[2] U. Pietch, V. Holý, and T. Baumbach, High-Resolution X-Ray Scattering: From Thin Films to Lateral Nanostructures (Springer Science & Business Media, New York, 2013), p. 408.

[3] P. F. Fewster, X-Ray Scattering from Semiconductors and Other Materials (World Scientific, London, 2015), p. 512.

[4] M. Schmidbauer, X-ray Diffuse Scattering from Self-Organized Mesoscopic Semiconductor Structures (Springer, Berlin, Heidelberg, 2010), p. 202.

[5] M. A. Krivoglaz, Diffraction of X-Rays and Thermal Neutrons in Imperfect Crystals (Springer, Berlin, New York, 1996), p. 466.

[6] A. Authier, Dynamical Theory of X-ray Diffraction (Oxford University Press, Oxford, 2004), p. 674.

[7] P. K. Shreeman and R. J. Matyi, J. Appl. Crystallogr. 43, 550 (2010).

[8] V. Soltwisch, A. Haase, J. Wernecke, J. Probst, M. Schoengen, S. Burger, M. Krumrey, and F. Scholze, Phys. Rev. B 94, 035419 (2016).

[9] V. I. Punegov, Phys.-Usp. 58, 419 (2015).

[10] V. B. Molodkin, S. I. Olikhovskii, E. N. Kislovskii, E. G. Len, and E. V. Pervak, Phys. Status Solidi B 227, 429 (2001).

[11] S. I. Olikhovskii, V. B. Molodkin, E. N. Kislovskii, E. G. Len, and E. V. Pervak, Phys. Status Solidi B 231, 199 (2002).

[12] V. B. Molodkin, S. I. Olikhovskii, E. N. Kislovskii, T. P. Vladimirova, E. S. Skakunova, R. F. Seredenko, and B. V. Sheludchenko, Phys. Rev. B 78, 224109 (2008).

[13] Y. Zorenko, V. Gorbenko, V. Savchyn, T. Zorenko, A. Fedorov, and O. Sidletskiy, J. Cryst. Growth 401, 532 (2014).

[14] T. Wehlus, T. Körner, S. Nowy, J. Frischeisen, H. Karl, B. Stritzker, and W. Brütting, Phys. Status Solidi A 208, 264–275 (2011).

[15] M. Nikl and A. Yoshikawa, Adv. Opt. Mater. 3(4), 463–481 (2015).

[16] Y. Zhu, G. Qiu, and C. S. Tsai, J. Appl. Phys. 111, 07A502 (2012).

[17] A. I. Popov, D. I. Plokhov, and A. K. Zvezdin, Phys. Rev. B 90, 214427 (2014).

[18] A. Rückriegel, P. Kopietz, D. A. Bozhko, A. A. Serga, and B. Hillebrands, Phys. Rev. B 89, 184413 (2014).

[19] U. V. Valiev, S. A. Rakhimov, N. I. Juraeva, R. A. Rupp, L. Zhao, Z. Wang, Z. Y. Zhai, J. B. Gruber, and G. W. Burdick, Phys. Status Solidi B 247, 163–169 (2010).

[20] K. Ghimire, H. F. Haneef, R. W. Collins, and N. J. Podraza, Phys. Status Solidi B 252, 2191–2198 (2015).

[21] M. Niyaifar, H. Mohammadpour, A. Aezami, and J. Amighian, Phys. Status Solidi B 253, 554–558 (2016).

[22] P.-H. Wu and S.-Y. Huang, Phys. Rev. B 94, 024405 (2016).

[23] C. Sun, T. Nattermann, and V. L. Pokrovsky, Phys. Rev. Lett. 116, 257205 (2016).

[24] Z. Wang, C. Tang, R. Sachs, Y. Barlas, and J. Shi, Phys. Rev. Lett. 114, 016603 (2015).

[25] J. B. S. Mendes, O. A. Santos, L. M. Meireles, R. G. Lacerda, L. H. Vilela-Leão, F. L. A. Machado, R. L. Rodríguez-Suárez, A. Azevedo, and S. M. Rezende, Phys. Rev. Lett. 115, 226601 (2015).

[26] P. Gruszecki, Yu. S. Dadoenkova, N. N. Dadoenkova, I. L. Lyubchanskii, J. Romero-Vivas, K. Y. Guslienko, and M. Krawczyk, Phys. Rev. B 92, 054427 (2015).

[27] A. Kehlberger, K. Richter, M. C. Onbasli, G. Jakob, D. H. Kim, T. Goto, C. A. Ross, G. Götz, G. Reiss, T. Kuschel, and M. Kläui, Phys. Rev. Appl. 4, 014008 (2015).

[28] F. W. Aldbea and N. B. Ibrahim, J. Mater. Sci. Appl. 1, 185 (2015).

[29] Yu. Zorenko, V. Gorbenko, T. Zorenko, O. Sidletskiy, A. Fedorov, P. Bilski, and A. Twardak, Phys. Status Solidi RRL 9, 489–493 (2015); Erratum: Phys. Status Solidi RRL 9, 607 (2015).

[30] C. R. Stanek, C. Jiang, S. K. Yadav, K. J. McClellan, B. P. Uberuaga, D. A. Andersson, and M. Nikl, Phys. Status Solidi B 250, 244–248 (2013).

[31] A. Sposito, G. B. G. Stenning, S. A. Gregory, P. A. J. de Groot, and R.t W. Eason, Thin Solid Films 568, 31 (2014).

[32] P. Görnert, T. Aichele, A. Lorenz, R. Hergt, and J. Taubert, Phys. Status Solidi A 201, 1398–1402 (2004).

[33] C. Ronning, C. Borschel, S. Geburt, R. Niepelt, S. Müller, D. Stichtenoth, J.-P. Richters, A. Dev, T. Voss, L. Chen, W. Heimbrodt, C. Gutsche, and W. Prost, Phys. Status Solidi B 247, 2329–2337 (2010).

[34] K. B. Modi and P. U. Sharma, Radiat. Eff. Defects Solids 169, 723–739 (2014).

[35] I. V. Antonova, Phys. Status Solidi B 244, 443–447 (2007).

[36] Yu. V. Kapitonov, P. Yu. Shapochkin, Yu. V. Petrov, Yu. P. Efimov, S. A. Eliseev, Yu. K. Dolgikh, V. V. Petrov, and V. V. Ovsyankin, Phys. Status Solidi B 252, 1950–1954 (2015).

[37] J. Geurts, M. Schumm, M. Koerdel, C. Ziereis, S. Müller, C. Ronning, E. Dynowska, Z. Gołacki, and W. Szuszkiewicz, Phys. Status Solidi B 247, 1469–1471 (2010).

[38] E. Wendler, N. A. Sobolev, A. Redondo-Cubero, and K. Lorenz, Phys. Status Solidi B 253, 2099–2109 (2016).

[39] J. England and W. Möller, Nucl. Instrum. Methods Phys. Res. B 365, 105–109 (2015).

[40] J. E. Thomas, T. O. Baldwin, and P. H. Dederichs, Phys. Rev. B 3, 1167 (1971).

[41] K. Karsten and P. Ehrhart, Phys. Rev. B 51, 10508 (1995).

[42] B. C. Larson, J. Appl. Crystallogr. 8, 150 (1975).

[43] P. Ehrhart, J. Nucl. Mater. 216, 170–198 (1994).

[44] P. H. Dederichs, Phys. Rev. B 4, 1041 (1971).

[45] P. H. Dederichs, J. Phys. F: Met. Phys. 3(2), 471 (1973).

[46] B. C. Larson and F. W. Young, Phys. Status Solidi A 104, 273 (1987).

[47] K. Nordlund, U. Beck, T. H. Metzger, and J. R. Patel, Appl. Phys. Lett. 76, 846 (2000).

[48] K. Nordlund, P. Partyka, R. S. Averback, K. Robinson, and P. Ehrhart, J. Appl. Phys. 88, 2278 (2000).

[49] R. E. Stoller, F. J. Walker, E. D. Specht, D. M. Nicholson, R. I. Barabash, P. Zschack, and G. E. Ice, J. Nucl. Mater. A 367–370, 269–275 (2007).

[50] F. Rieutord, F. Mazen, S. Reboh, J. D. Penot, L. Bilteanu, J. P. Crocombette, V. Vales, V. Holy, and L. Capello, J. Appl. Phys. 113, 153511 (2013).

[51] J. Channagiri, A. Boulle, and A. Debelle, J. Appl. Crystallogr. 48, 252 (2015).

[52] D. Carbone, A. Biermanns, B. Ziberi, F. Frost, O. Plantevin, U. Pietsch, and T. H. Metzger, J. Phys.: Condens. Matter **21**, 224007 (2009).

[53] A. Richard, H. Palancher, É. Castelier, J.-S. Micha, M. Gamaleri, G. Carlot, H. Rouquette, P. Goudeau, G. Martin, F. Rieutord, J. P. Piron, and P. Garcia, J. Appl. Crystallogr. **45**, 826–833 (2012).

[54] R. Lang, A. S. de Menezes, A. O. dos Santos, S. Reboh, E. A. Meneses, L. Amaral, and L. Cardoso, J. Appl. Crystallogr. **46**, 1796–1804 (2013).

[55] B. Khanbabaee, A. Biermanns, S. Facsko, J. Grenzer, and U. Pietsch, J. Appl. Crystallogr. **46**, 505–511 (2013).

[56] M. Sztucki T. H. Metzger I. Kegel, A. Tilke, J. L. Rouvière, D. Lübbert, J. Arthur, and J. R. Patel, J. Appl. Phys. **92**, 3694 (2002).

[57] B. Khanbabaee, S. Facsko, S. Doyle, and U. Pietsch, Appl. Phys. Lett. **105**, 163101 (2014).

[58] M. Ibrahim, É. Castelier, H. Palancher, M. Bornert, S. Caré, and J.-S. Micha, J. Appl. Crystallogr. **48**, 990–999 (2015).

[59] M. Karlušić, S. Bernstorff, Z. Siketić, B. Šantić, I. Bogdanović-Radović, M. Jakšić, M. Schleberger, and M. Buljan, J. Appl. Crystallogr. **49**, 1704 (2016).

[60] A. Yu. Nikulin, O. Sakata, H. Hashizume, and P. V. Petrashen, J. Appl. Crystallogr. **27**, 338–344 (1994).

[61] M. Yoon, B. C. Larson, J. Z. Tischler, T. E. Haynes, J.-S. Chung, G. E. Ice, and P. Zschack, J. Appl. Phys. **75**, 2791 (2000).

[62] P. V. Petrashen, Fiz. Tverd. Tela **17**, 2814 (1975).

[63] A. M. Afanasev, M. V. Kovalchuk, E. K. Kovev, and V. G. Kohn, Phys. Status Solidi A **42**, 415 (1977).

[64] R. N. Kyutt, P. V. Petrashen, and L. M. Sorokin, Phys. Status Solidi A **60**, 381 (1980).

[65] V. S. Speriosu, J. Appl. Phys. **52**, 6094 (1981).

[66] M. Servidori, Nucl. Instrum. Methods Phys. Res. B **19–20**, 443 (1987).

[67] J. G. E. Klappe and P. F. Fewster, J. Appl. Crystallogr. **27**, 103–110 (1994).

[68] S. Milita and M. Servidori, J. Appl. Crystallogr. **28**, 666–672 (1995).

[69] A. Parisini, S. Milita, and M. Servidori, Acta Crystallogr. A **52**, 302–311 (1996).

[70] A. Boulle and A. Debelle, J. Appl. Crystallogr. **43**, 1046–1052 (2010).

[71] Yu. N. Belyaev and A. V. Kolpakov, Phys. Status Solidi A **76**, 641 (1983).

[72] C. R. Wie, T. A. Tombrello, and T. Vreeland Jr., J. Appl. Phys. **59**, 3743 (1986).

[73] M. Dimer, E. Gerdau, R. Rüffer, H. D. Rüter, and W. Sturhahn, J. Appl. Phys. **79**, 9090 (1996).

[74] P. K. Shreeman and R. J. Matyi, Phys. Status Solidi A **208**, 2533 (2011).

[75] A. Yu. Nikulin, Phys. Rev. B **57**, 11178 (1998).

[76] J. Channagiri, A. Boulle, and A. Debelle, Nucl. Instrum. Methods Phys. Res. B **327**, 9 (2014).

[77] C. Glorieux and E. Zolotoyabko, J. Appl. Crystallogr. **34**, 336–342 (2001).

[78] L. Bleicher, J. M. Sasaki, R. V. Orloski, L. P. Cardoso, M. A. Hayashi, and J. W. Swart, Comput. Phys. Commun. **160**, 158–165 (2004).

[79] O. S. Skakunova, Metallofiz. Noveish. Tekhnol. **37**, 555 (2015).

[80] B. Strocka, P. Holst, and W. Tolksdorf, Philips J. Res. **33**, 186 (1978).

[81] Yu. P. Vorob'ev, Metallofiz. Noveish. Tekhnol. **26**, 27 (2004).

[82] V. M. Pylypiv, S. I. Olikhovskii, T. P. Vladimirova, O. S. Skakunova, V. B. Molodkin, B. K. Ostafiichuk, Ye. M. Kislovskii, O. V. Reshetnyk, S. V. Lizunova, and O. Z. Garpul, Metallofiz. Noveish. Tekhnol. **33**, 1147 (2011).

[83] M. Bonnet, A. Delapalme, H. Fuess, and M. Thomas, Acta Crystallogr. B **31**, 2233 (1975).

[84] V. M. Pylypiv, B. K. Ostafyjchuk, T. P. Vladymyrova, Ye. M. Kislovskii, V. B. Molodkin, S. I. Olikhovskii, O. V. Reshetnik, O. S. Skakunova, and S. V. Lizunova, Nanosist. Nanomater. Nanotehnol. (Ukraine) **9**, 375 (2011).

[85] V. M. Pylypiv, T. P. Vladimirova, I. M. Fodchuk, B. K. Ostafiichuk, Ye. M. Kyslovskyy, V. B. Molodkin, S. I. Olikhovskii, O. V. Reshetnyk, O. S. Skakunova, V. V. Lizunov, and O. Z. Garpul', Phys. Status Solidi A **208**, 2558 (2011).

[86] T. P. Vladimirova, V. M. Pylypiv, B. K. Ostafiichuk, Ye. M. Kislovskii, V. B. Molodkin, S. I. Olikhovskii, O. S. Skakunova, O. V. Reshetnyk, and S. V. Lizunova, Nanosist. Nanomater. Nanotehnol. (Ukraine) **9**, 505 (2011).

[87] S. Geller and M. A. Gilleo, J. Phys. Chem. Solids **3**, 30 (1957).

[88] S. Vélez, A. Bedoya-Pinto, W. Yan, L. E. Hueso, and F. Casanova, Phys. Rev. B **94**, 174405 (2016).

[89] J. M. Wesselinowa and A. B. Dimitrov, Phys. Status Solidi B **244**, 2242 (2007).

[90] J. M. Wesselinowa, A. T. Apostolov, and S. Trimper, Phys. Status Solidi B **248**, 1658 (2011).

[91] M. Nastasi, J. W. Mayer, and J. K. Hirvonen, Ion-Solid Interactions: Fundamentals and Applications (Cambridge University Press, Cambridge, 2004).

[92] B. K. Ostafiichuk, V. D. Fedoriv, I. P. Yaremiy, O. Z. Garpul, V. V. Kurovets, and I. C. Yaremiy, Phys. Status Solidi A **208**, 2108 (2011).

[93] S. B. Ubizskii, A. O. Matkovskii, N. Mironova-Ulmane, V. Skvortsova, A. Suchocki, Y. A. Zhydachevskii, and P. Potera, Phys. Status Solidi A **177**, 349 (2000).

[94] P. Potera, Comput. Methods Sci. Technol. **13**, 47–51 (2007).

[95] O. Yu. Goncharov, Crystallogr. Rep. **48**, 1–7 (2003).

[96] S. Kostić, Z. Ž. Lazarević, V. Radojević, A. Milutinović, M. Romčević, N. Ž. Romčević, and A. Valčić, Mater. Res. Bull. **63**, 80–87 (2015).

[97] J. Dong and K. Lu, Phys. Rev. B **43**, 8808 (1990).

[98] L. J. Graham and R. Chang, J. Appl. Phys. **41**, 2247 (1970).

[99] J. Rabier, P. Veyssière, and J. Grilhé, Phys. Status Solidi A **35**, 259 (1976).

[100] B. Pavis, G. Rivaud, J. Rabier, and P. Veyssière, Phys. Status Solidi A **54**, K85 (1979).

[101] P. Veyssière, Radiation Effects **74**(1–4), 1–15 (1983).

[102] C. D. Brandle, D. C. Miller, and J. W. Nielsen, J. Cryst. Growth **12**(3), 195–200 (1972).

[103] D. Peizhen and Q. Jingwen, J. Cryst. Growth **82**(4), 579 (1987).

[104] J.-G. Li and Y. Sakka, Sci. Technol. Adv. Mater. **16**, 014902 (2015).

[105] O. Yu. Goncharov, Crystallographiya (Ukraine) **48**, 7 (2003).

[106] H. Donnerberg and C. R. A. Catlow, J. Phys.: Condens. Matter **5**, 2947 (1993).

[107] F. Maglia, V. Buscaglia, S. Gennari, P. Ghigna, M. Dapiaggi, A. Speghini, and M. Bettinelli, J. Phys. Chem. B **110**, 6561 (2006).

[108] C. Milanese, V. Buscaglia, F. Maglia, and U. Anselmi-Tamburini, Chem. Mater. **16**, 1232 (2004).

[109] H. Donnerberg and C. R. A. Catlow, J. Phys.: Condens. Matter **5**, 2947 (1993).

[110] F. Maglia, V. Buscaglia, S. Gennari, P. Ghigna, M. Dapiaggi, A. Speghini, and M. Bettinelli, J. Phys. Chem. B **110**, 6561 (2006).

[111] C. Milanese, V. Buscaglia, F. Maglia, and U. Anselmi-Tamburini, Chem. Mater. **16**, 1232 (2004).

[112] H. L. Glass and M. T. Elliott, J. Cryst. Growth **27**, 253 (1974).

[113] G. B. Scott and J. L. Page, J. Appl. Phys. **48**, 1342 (1977).

[114] H. Donnerberg and C. R. A. Catlow, Phys. Rev. B **50**, 744 (1994).

[115] J.-Ch. Chen and Ch.-Ch. Hu, J. Cryst. Growth **249**, 245 (2003).

[116] M. Kučera, K. Nitsch, H. Štěpánková, M. Maryško, and P. Reiche, Phys. Status Solidi A **198**, 407–414 (2003).

[117] A. Sposito, S. A. Gregory, P. A. J. de Groot, and R. W. Eason, J. Appl. Phys. **115**, 053102 (2014).

[118] R. Peña-Garcia, A. Delgado, Y. Guerra, and E. Padrón-Hernández, Mater. Lett. **161**, 384–386 (2015).

[119] S. I. Yushchuk, Tech. Phys. **44**, 1454–1456 (1999).

[120] A. E. Clark and R. E. Strakna, J. Appl. Phys. **32**, 1172 (1961).

[121] O. S. Skakunova, V. M. Pylypiv, T. P. Vladimirova, S. I. Olikhovskii, V. B. Molodkin, B. K. Ostafiichuk, Ye. M. Kislovskii, O. V. Reshetnyk, and S. V. Lizunova, Metallofiz. Noveish. Tekhnol. **35**, 1595 (2013).

[122] J. F. Ziegler, J. P. Biersack, and U. Littmark, The Stopping and Range of Ions in Solids (Pergamon, New York, 1985), p. 321.

[123] O. S. Skakunova, V. M. Pylypiv, S. I. Olikhovskii, T. P. Vladimirova, B. K. Ostafiichuk, V. B. Molodkin, Ye. M. Kislovskii, O. V. Reshetnyk, O. Z. Garpul, A. V. Kravets, and V. L. Makivska, Metallofiz. Noveish. Tekhnol. **34**, 1325 (2012).

[124] C. Lu, K. Jin, L. K. Béland, F. Zhang, T. Yang, L. Qiao, L. Wang, H. Bei, H. M. Christen, R. E. Stoller, and L. Wang, Sci. Rep. **6**, 19994 (2016).

[125] A. Yu. Didyk, F. F. Komarov, L. A. Vlasukova, E. A. Gracheva, A. Hofman, V. N. Yuvchenko, R. Wiśniewski, and T. Wilczyńska, Nukleonika **53**, 77 (2008).

[126] V. O. Kotsyubynskyy, V. M. Pylypiv, B. K. Ostafiichuk, I. P. Yaremiy, O. Z. Garpul, O. S. Skakunova, V. B. Molodkin, and S. I. Olikhovskyy, Metallofiz. Noveish. Tekhnol. **36**, 1049 (2014).

[127] J. R. Beeler Jr., in: Radiation Effects Computer Experiments, Vol. 13 of Defects in Solids, series edited by S. Amelinckx, R. Gevers, and J. Nihoul (Elsevier, New York, 2012), p. 900.

[128] A. F. Calder, D. J. Bacon, A. V. Barashev, and Yu. N. Osetsky, Philos. Mag. **90**, 863 (2010).

[129] M. J. Caturla, N. Soneda, T. Diaz de la Rubia, and M. Fluss, J. Nucl. Mater. **351**(1), 78–87 (2006).

[130] A. V. Korchuganov, V. M. Chernov, K. P. Zolnikov, D. S. Kryzhevich, and S. G. Psakhie, Inorg. Mater. Appl. Res. **7**, 648–657 (2016).

[131] V. M. Pylypiv, O. S. Skakunova, T. P. Vladimirova, Ye. M. Kyslovskii, B. K. Ostafiichuk, V. B. Molodkin, S. I. Olikhovskii, O. V. Reshetnyk, O. Z. Garpul, and V. L. Makivska, Metallofiz. Noveish. Tekhnol. **34**, 1451 (2012).

[132] V. M. Pylypiv, O. Z. Garpul, B. K. Ostafiichuk, V. O. Kotsubynskii, V. V. Kurovets, and O. Yu. Bonchik, Phys. Chem. Solid State **13**, 48 (2012).

[133] I. I. Syvorotka, D. Sugak, A. Wierzbicka, A. Wittlin, H. Przybylińska, J. Barzowska, A. Barcz, M. Berkowski, J. Domagała, S. Mahlik, M. Grinberg, C.-G. Ma, M. G. Brik, A. Kamińska, Z. R. Zytkiewicz, and A. Suchocki, J. Lumin. **164**, 31 (2015).

[134] K. B. Eidelman, K. D. Shcherbachev, N. Yu. Tabachkova, D. A. Podgornii, and V. N. Mordkovich, Nucl. Instrum. Methods Phys. Res. B **365**, 141–145 (2015).

[135] I. M. Fodchuk, I. I. Gutsuliak, V. V. Dovganiuk, A. O. Kotsyubynskiy, U. Pietsch, N. V. Pashniak, O. Yu. Bonchyk, I. M. Syvorotka, and P. M. Lytvyn, Appl. Opt. **55**(12), B144 (2016).

[136] P. Zaumseil and U. Winter, Phys. Status Solidi A **120**, 67–75 (1990).

[137] A. Debelle, J. Channagiri, L. Thomé, B. Décamps, A. Boulle, S. Moll, F. Garrido, M. Behar, and J. Jagielski, J. Appl. Phys. **115**, 183504 (2014).

[138] B. K. Ostafiychuk, I. P. Yaremiy, S. I. Yaremiy, V. D. Fedoriv, U. O. Tomyn, M. M. Umantsiv, I. M. Fodchuk, and V. P. Kladko, Crystallogr. Rep. **58**, 1017 (2013).

[139] S. Pellegrino, J.-P. Crocombette, A. Debelle, T. Jourdan, P. Trocellier, and L. Thomé, Acta Mater. **102**, 79 (2016).

[140] A. Biermanns, A. Hanisch, J. Grenzer, T. H. Metzger, and U. Pietsch, Phys. Status Solidi A **208**, 2608–2611 (2011).

[141] B. Nunes, N. Franco, A. M. Botelho do Rego, E. Alves, and R. Colaç, Nucl. Instrum. Methods Phys. Res. B **365**, 39–43 (2015).

[142] M. Fialho, S. Magalhães, M. P. Chauvat, P. Ruterana, K. Lorenz, and E. Alves, J. Appl. Phys. **120**, 165703 (2016).

[143] Y. Zhang, A. Debelle, A. Boulle, P. Kluth, and F. Tuomisto, Curr. Opin. Solid State Mater. Sci. **19**(1), 19–28 (2015).